Data, Innovation, and Science Cluster

# Swarm-PRISM Validation Report

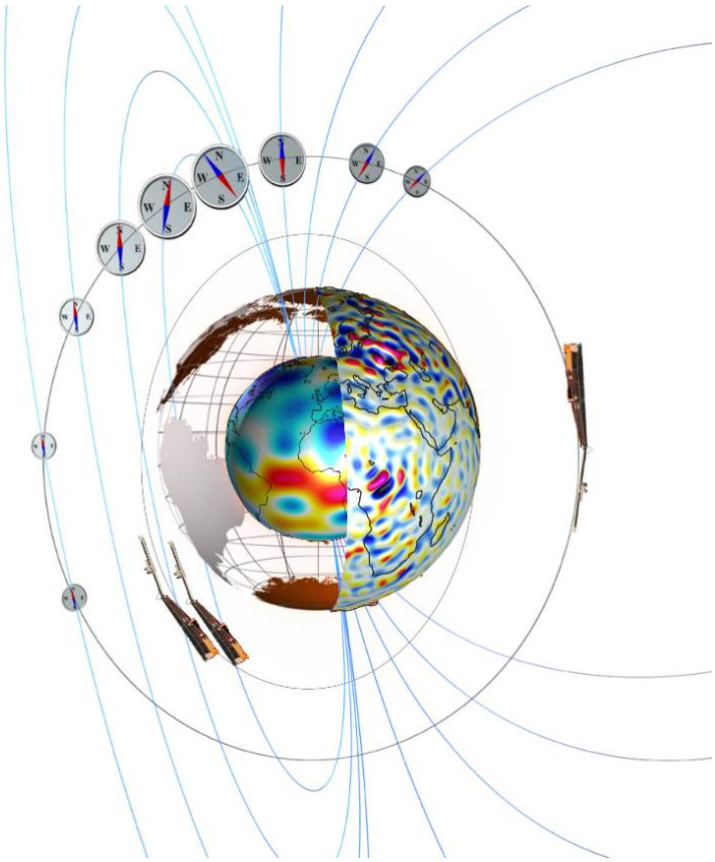

**Doc. no: SW-DS-GFZ-GS-007, Rev: 3, 25 Jun 2021**

Prepared:

Balazs Heilig — Date 25 Jun 2021

Scientist

Approved: Claudia Stolle — Digitally signed by Claudia Stolle Date: 2021.06.28 16:29:26 +02'00'

Claudia Stolle — Date 25 Jun 2021

Team Leader

Checked: Guram Kervalishvili — DN: cn=Guram Kervalishvili, o=GFZ German Research Centre for Geosciences, email=gmk@gfz-potsdam.de, c=DE Date: 2021.06.28 16:09:25 +02'00'

Guram Kervalishvili — Date 25 Jun 2021

Scientist

# Record of Changes

| Reason | Description | Rev | Date |
|---|---|---|---|
| Initial vers. | Released. | 1 dA | 09 Nov 2020 |
| Signature | | 1 | 10 Nov 2020 |
| Updated input from GFZ | Section 5 with including all subsections was moved to [AD-3].<br>Document text has been updated and corrected with minor changes.<br>Figure 4.3 – Figure 4.9, Figure 4.11 – Figure 4.15, Figure 4.23 – Figure 4.28, Figure 5.4, Figure 5.7, Figure 5.10, Figure 5.12 and Figure 5.13 have been updated including several new figures.<br>Table 4-1 – Table 4-6 have been updated. | 2 dA | 29 Mar 2021 |
| Signature | | 2 | 31 Mar 2021 |
| Email from Klaus to Guram: 09.06.2021 10h05 | Minor text updates according to reviewers' comments. | 3 dA | 18 Jun 2021 |
| Signature | | 3 | 25 Jun 2021 |

# Table of Contents

# List of Figures

## List of Tables

# 1 Introduction

## 1.1 Scope and applicability

This document comprises the summary and main results of the validation activity the Swarm Level 2 (L2) PRISM products in response to the requirements of [AD-1]. Swarm PRISM includes the following products [AD-2]:

- **MITx_LP_2F** – Characterisation of the Mid-latitude Ionospheric Trough based on Langmuir probe observations
- **MITxTEC_2F** – Characterisation of the Mid-latitude Ionospheric Trough based on GNSS TEC observations
- **PPIxFAC_2F** – Midnight Plasmapause Index and equatorward boundary of small-scale field aligned currents

The Swarm-PRISM Product Definition document [AD-2] is available in the SVN folder: https://smart-svn.spacecenter.dk/svn/smart/SwarmDISC/DISC_Projects/ITT2_2_PRISM/Deliverables/.

Current or updated version of this document is available in the SVN folder: https://smart-svn.spacecenter.dk/svn/smart/SwarmDISC/DISC_Projects/ITT2_2_PRISM/Deliverables/.

# 2 Applicable and Reference Documentation

## 2.1 Applicable Documents

The following documents are applicable to the definitions within this document.

[AD-1] SW-OF-GFZ-GS-122_2-2_PRISM_Proposal, Proposal for Swarm DISC ITT 2.2, Swarm-PRISM – Plasmapause Related boundaries in the topside Ionosphere as derived from Swarm Measurements.

[AD-2] SW-DS-GFZ-GS-003_2-2_PRISM_PDD, Product Definition Document.

[AD-3] SW-DS-GFZ-GS-006_2-2_PRISM_DPA, Description of the Processing Algorithms.

## 2.2 Reference Documents

The following documents contain supporting and background information to be taken into account during the activities specified within this document.

[RD-1] Heilig, B. and Lühr, H. (2013), New plasmapause model derived from CHAMP field-aligned current signatures, Ann. Geophys., 31, 529-539, doi: 10.5194/angeo-31-529-2013.

[RD-2] Heilig, B. and Lühr, H. (2018), Quantifying the relationship between the plasmapause and the inner boundary of small-scale field-aligned currents, as deduced from Swarm observations, Ann. Geophys. 36, 595-607, doi: 10.5194/angeo-36-595-2018.

[RD-3] Pedersen, A., et al. (2008), Electron density estimations derived from spacecraft potential measurements on Cluster in tenuous plasma regions, J. Geophys. Res., 113, A07S33, doi: 10.1029/2007JA012636.

[RD-4] Fu, H. S., J. B. Cao, B. Yang, and H. Y. Lu (2011), Electron loss and acceleration during storm time: The contribution of wave-particle interaction, radial diffusion, and transport processes, J. Geophys. Res., 116, A10210, doi: 10.1029/2011JA016672.

[RD-5] Del Corpo, A., Vellante, M., Heilig, B., Pietropaolo, E., Reda, J., & Lichtenberger, J. ( 2020). An Empirical Model for the Dayside Magnetospheric Plasma Mass Density Derived From EM-MA Magnetometer Network Observations. Journal of Geophysical Research: Space Physics, 125, e2019JA027381, doi: 10.1029/2019JA027381.

[RD-6] Virtual research platform (VirES), https://vires.services.

[RD-7] Heilig, B., C. Stolle, G. Kervalishvili, J. Rauberg, Y. Miyoshi, F. Tsuchiya, A. Kumamoto, Y. Kasahara, M. Shoji, S. Nakamura, M. Kitahara, I. Shinohara (2021), Relation between the Plasma-pause Dynamics and the Mid-latitude Ionospheric Trough as Observed in the Topside Ionosphere by Swarm, submitted to Journal of Geophysical Research: Space Physics.

## 2.3 Abbreviations

A list of acronyms and abbreviations used by Swarm partners can be found here. Any acronyms or abbreviations not found on the online list but used in this document can be found below.

| ***Acronym*** ***or abbreviation*** | ***Description*** |
|---|---|
| EW | EquatorWard |
| IGRF | International Geomagnetic Reference Field |
| L-value | The McIlwain L-parameter, distance of the field line apex from the centre of the Earth measured in Earth radii |
| MIT | Mid-latitude Ionospheric Trough |
| N | North, northern |
| Ne | electron number density |
| PP | PlasmaPause |
| PRISM | Plasmapause Related boundaries in the topside Ionosphere as derived from Swarm Measurements (this project) |
| PW | PoleWard |
| S | South, southern |
| SETE | Sub-auroral Temperature Enhancement |
| SSFAC | Small-Scale FAC |
| Te | electron temperature |
| WSA | Weddell-See Anomaly |

# 3 Background and rationale

The position of the plasmapause (PP) is a key parameter in space weather. The variation of the PP location is a very sensitive indicator of geomagnetic activity. There are many space phenomena (e.g., cold plasma and energetic particle populations, various ULF-ELF-VLF wave populations) separated spatially by the PP, as well as a number of space processes (e.g., wave generation and grow mechanisms, wave propagation, various resonances, particle precipitation, high-latitude magnetosphere-ionosphere coupling processes etc.) that are dynamically linked to the location of the plasmapause. The Swarm-PRISM products [AD-2] contribute to the characterisation of some of the PP related phenomena in the topside ionosphere. These are the mid-latitude ionospheric trough (MIT) derived from electron density and temperature measurements of the Langmuir probe and as a separate product, also from GPS TEC estimates, as well as the equatorward boundary of small-scale field-aligned currents (SSFACs) leading to an index that is also used to derive a proxy of the midnight position of the plasmapause. The following background information where no specific reference is given comes from [RD-1] [RD-2] [RD-7].

The MIT appears as a few-degree-wide depleted zone, where electron density (Ne) drops typically by orders of magnitude, primarily observable on the dark hemisphere. MIT is often associated with a plasma flow stagnation zone between the convection dominated plasma of the outer magnetosphere and the plasmaspheric plasma co-rotating with the Earth. MIT also appears in GPS TEC measurements. An elevated Te (SETE – Sub-auroral Temperature Enhancement) is typically observed near the trough minimum, which is believed to be caused by precipitation or frictional heating or decreased cooling (due to decreased density). The MIT equatorward/poleward edge has been found closely related to the ionospheric footprint of the PP/the auroral oval, respectively.

A new PP location proxy based on small-scale FAC signatures observed at LEO was introduced by [RD-1] [RD-2]. It was found that a very close coincidence exists between the PP position and the equatorward boundary of sub-auroral SSFACs (as mapped onto the magnetic equatorial plane along IGRF field lines) in the post-midnight MLT sector. The quiet plasmasphere is shielded from the electric field that drives FACs connected to the outer magnetosphere. During disturbed times, the new PP is formed in the post-midnight sub-auroral zone, where the conductivity is low compared to the auroral zone. To maintain current continuity through the conductivity contrast, the E-field grows across the lower-conductivity sub-auroral region. The elevated E-field drives the sub-auroral ion drift, contributes to the increase of FAC density outside the PP, moreover, mapped deep into the magnetosphere along the field lines this E-field also contributes to the erosion of the plasmasphere and the formation of the fresh PP.

All the three PRISM products, the MIT location (LP- and TEC-based version) and the midnight PP index, are provided as daily files separately for the three individual Swarm satellites. Each file contains records for the location of the boundaries and their characteristics, i.e., up to four crossings per orbit per boundary type. All products are visualised in the VirES environment [RD-6], where they can be compared to time series of other Swarm products, such as electron density and temperature, TEC, or the auroral AEBS products.

# 4 Validation of products

This document summarises the result and outcome of the PRISM validation activity. The goal of the validation is twofold: to validate the individual products characterising the corresponding phenomena (MIT and SSFAC boundary) as well as to validate the use of the products in estimating the location of the PP. To achieve these goals, for each product first, the observations of the closely separated, side-by-side flying A and C satellites are compared. This is followed by a statistical verification to test if the well-known behaviour of the investigated phenomenon can be deduced from the product. As a next step, each product is compared to the other two obtained from the measurements of the same satellite (co-located, simultaneous observations), since a strong coupling is expected between all these boundaries.

The product content is defined in [AD-2], while the product parameters including the boundaries as well as their derivation are described in [AD-3].

An important task of the validation is the definition of the quality flags that yields quantified measures of the product quality. Several quality flags are defined for every single boundary position. The quality flags are based on the time history or evolution of the considered boundary, the distance between the three boundaries, as well as from the auroral oval (AOB product), the circumstances of the observation (location, MLT, solar zenith angle, a region where the MIT-detection is affected by the Weddell-See-Anomaly). Based on the complete set of the flags the main flag is defined to account for the overall quality of the product record.

The validation of the PRISM products as potential indicators of the PP location is carried out by comparing the PRISM boundaries to PP observations derived from in-situ observation of magnetospheric electron density. The reference magnetospheric data set will be introduced in section 5, then the outcome of this work is summarised.

## 4.1 MITx_LP_2F

### 4.1.1 Verification

As a verification of the efficiency of the detection, first, the MIT related Ne minima and edges, as well as Te peaks and peak boundaries are plotted over a 2D Ne (Figure 4.1) and Te map (Figure 4.2). A ten-day interval around autumn equinox (1-10 Oct, 2015) is chosen, when there is a good chance to detect the MIT on both hemispheres. On the night side, the MLT of Swarm A during this interval was in the 2-6 MLT range. As shown in Figure 4.1, under these circumstances, the MIT could have been mostly successfully detected. The MIT minima are shown by downward triangles, the MIT edges by + signs. There were hardly any orbits in this interval when the detection failed. The triangles are coloured corresponding to the quality of the detection (see later). The highest quality detections are black, the still good detections are blue (e.g., the 4th and 5th on the S hemisphere), questionable ones are magenta (the very last on the S hemisphere), while the likely false positive detections are crossed in red (e.g., near the end of MJD 5753 on both hemispheres). The MIT edge positions also fairly agree with the background Ne map.

Figure 4.2 presents the SETE detections plotted over the Te maps. In the same equinox interval, the Te peak detections were also mostly successful. The SETE boundaries are also reasonable in most cases. The PW boundary is so close to the peak position that they are in most of the cases hardly distinguishable. In a few cases, especially in the S hemisphere, the EW boundary is detected at very low latitudes, where the Te contrast is sharper than at the true boundaries. This indicates that the detection of especially the EW boundary of the SETE can be problematic.

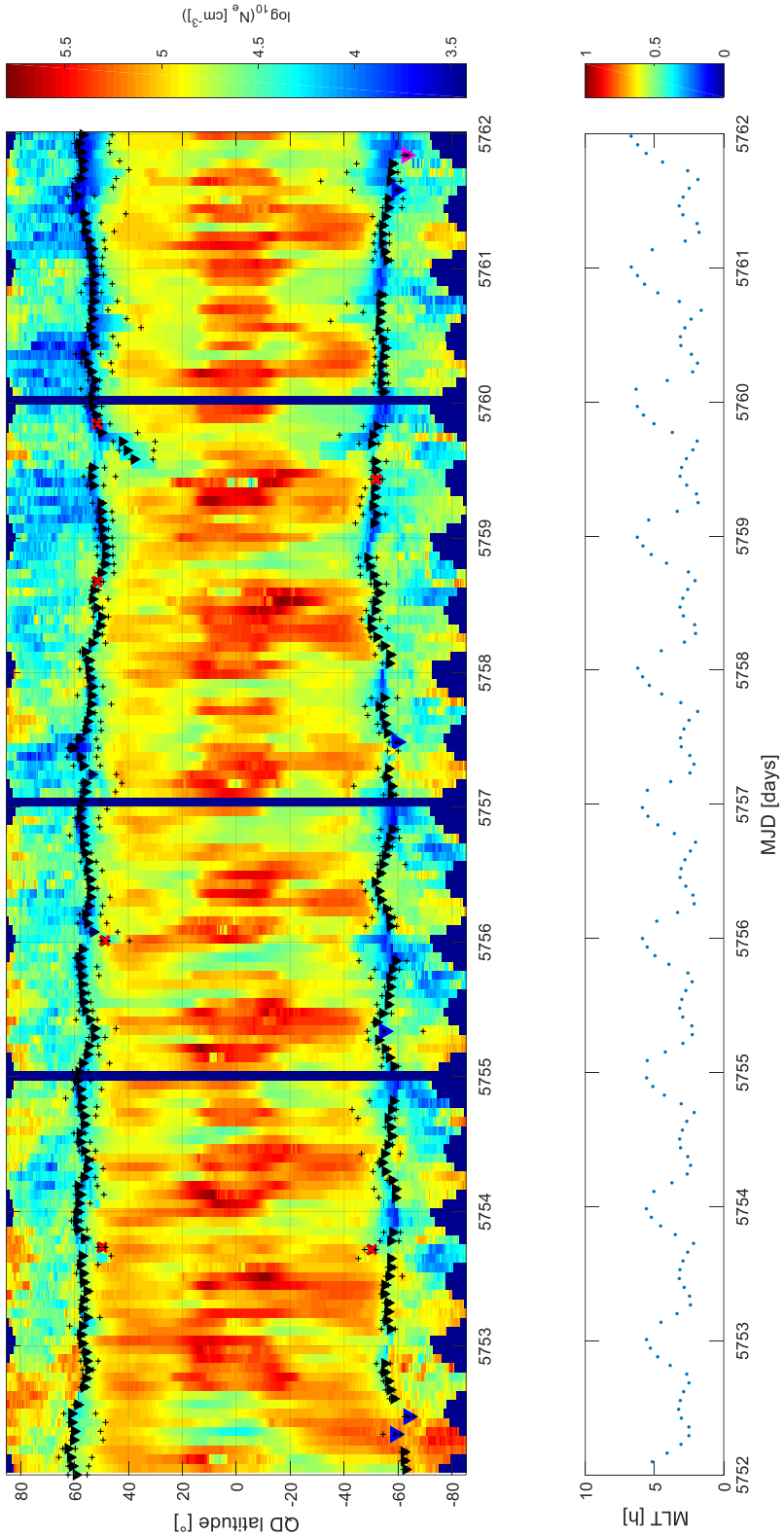


**Figure 4.1** (top) MITx_LP MIT minima (downward triangles), poleward and equatorward edges (black +) plot-ted over the LP log(Ne), (bottom) MLT at the equatorial crossing. Highest quality (main quality flag = 3) detections (minima) are shown in black, fair/poor quality (flagged by 2/1) are shown in blue/magenta, while likely false positives are crossed in red.

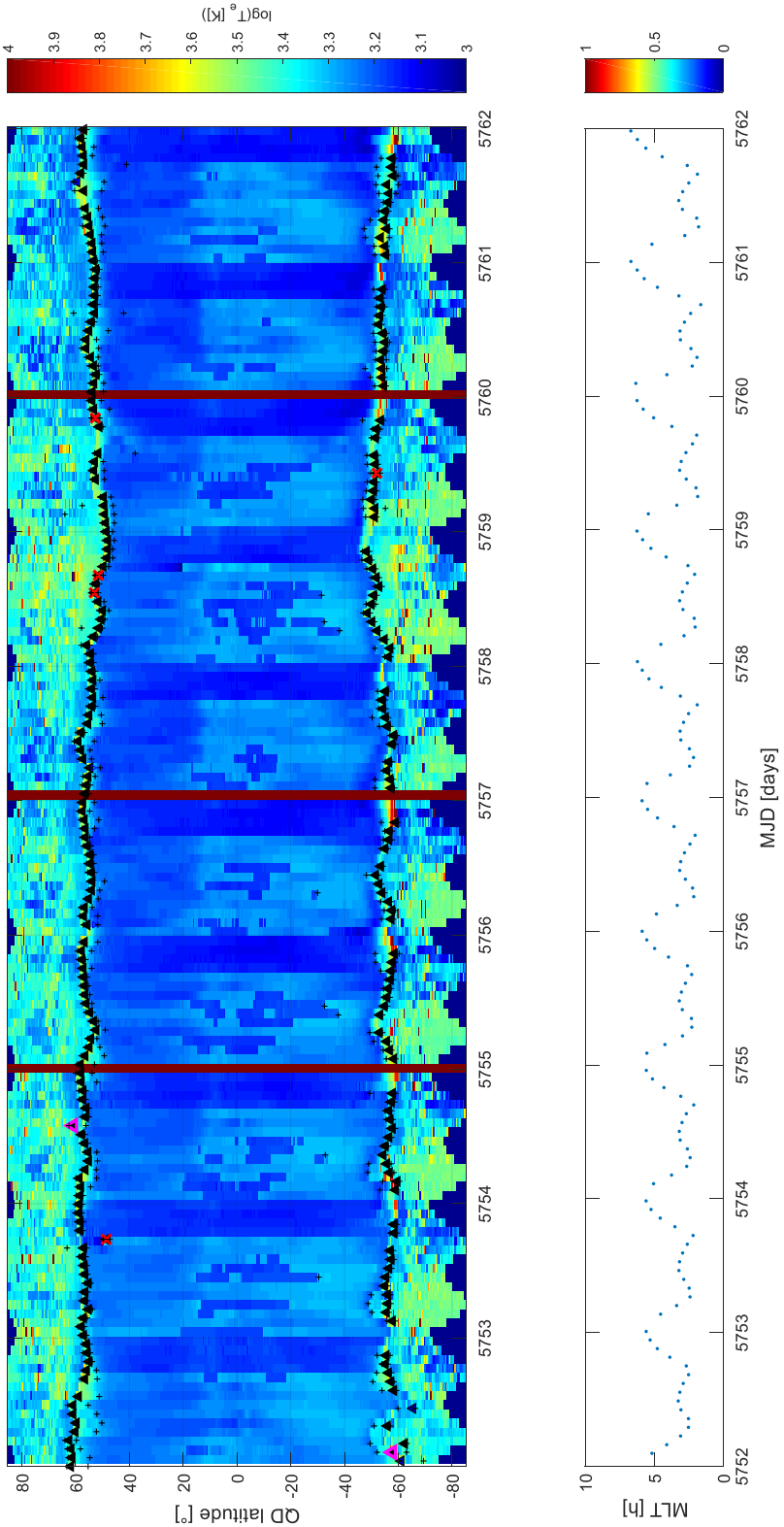


**Figure 4.2** (top) MITx_LP SETE maxima (upward triangles) and poleward and equatorward edges (black +) plotted over the LP log(Te), (bottom) MLT at the equatorial crossing. Highest quality (main quality flag = 3) detections (minima) are shown in black, fair/poor quality (flagged by 2/1) are shown in blue/magenta, while likely false positives are crossed in red.

It is also noted, that for both the MIT and SETE detections some likely good detections were erroneously qualified as likely false positive ones. This means that in these cases at least, the qualification procedure (discussed later) proved to be too strict.

### 4.1.2 Comparison between Swarm A and C

In Figure 4.3 MIT observations of Swarm A and C are compared. In 2015 the two satellites flew side by side, separated by 1°–1.5° in longitude. Since the longitudinal extension of the MIT covers at least the night side under favourable conditions, at least for the trough minimum and Te peak position a general good correspondence is expected, and thus these comparisons can be used to assess the accuracy of the observations.

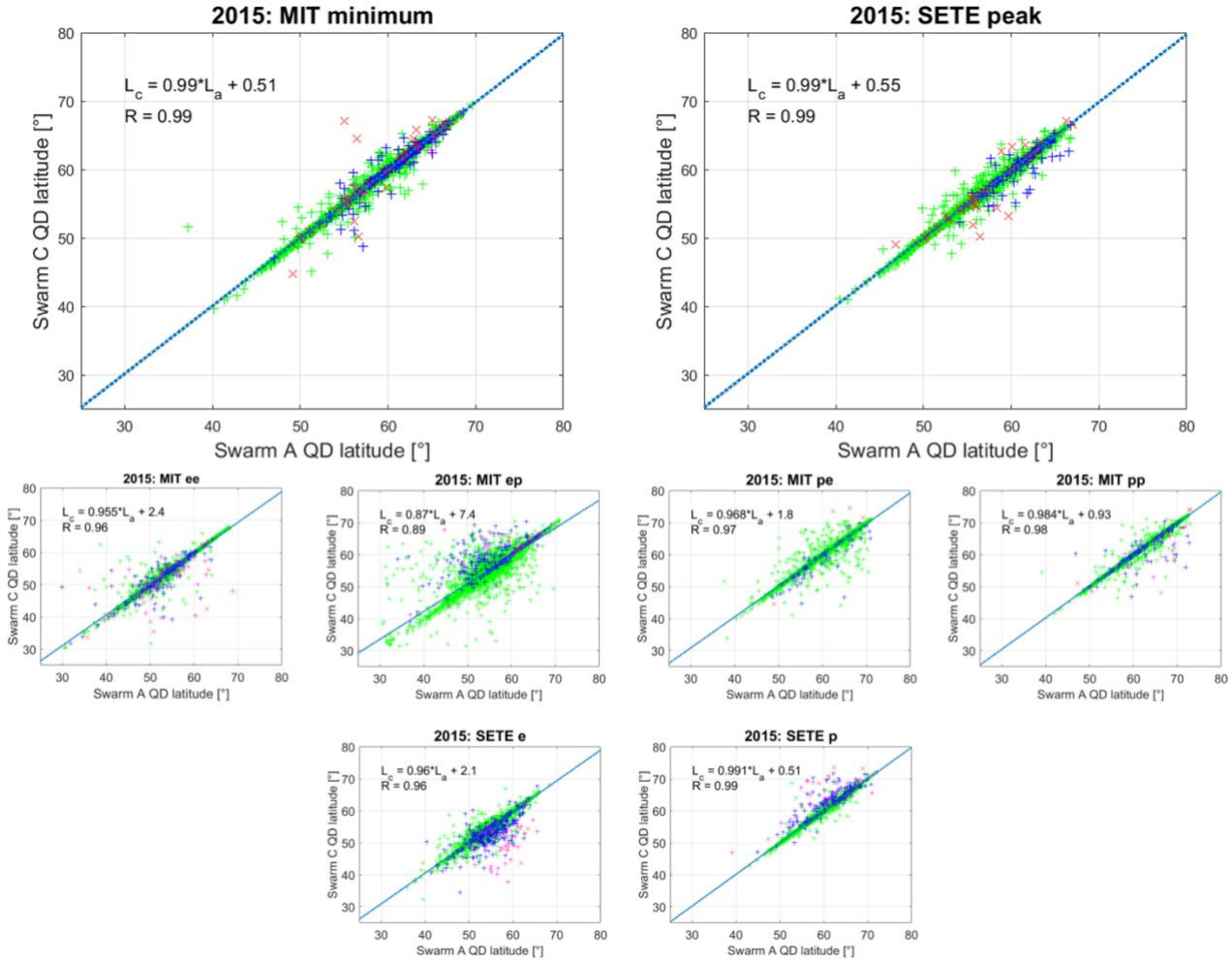


**Figure 4.3** Comparison of MIT minimum, SETE peak, MIT ee, MIT ep, MIT pe, MIT pp; SETE e, SETE p (see the text for their definition) positions as observed by Swarm A and C, all observations in 2015.

In Figure 4.3, all eight MIT boundaries as observed by the two satellites are compared. In the top row, the MIT minima, and SETE peak locations are compared. In each case the absolute values are plotted, hence observations made in both hemispheres are involved. Symbols are coloured according to the quality flag of the boundary observations of Swarm C, while Swarm C observations were always compared to the highest

quality Swarm A observations. Green indicates the highest quality Swarm C observations, followed by blue and magenta, while red depicts the detections that are likely false positives. As the comparisons show, there is a general good agreement between A and C observations, however, with a not negligible spread. The spread at least in part can be attributed to the small-scale variations embedded in the medium-scale MIT structure. On the other hand, scatter plots may be misleading, since coincident points cover each other. The correlation strength between the highest quality values is > 0.95 for all boundaries, except from MIT_ep (r = 0.87). Also, the linear fit on the highest quality data is close to y = 1.00*x + 0 for most of the boundaries.

The similarity between the Swarm A and C data sets can be better assessed from the distribution of their differences. Figure 4.4 presents the histograms of the differences, while Table 4-1 lists the standard deviations and the median absolute deviations calculated from the same samples. Again, only the highest quality values are considered. For the MIT minimum position, for the overwhelming majority (> 95%) of all cases, Swarm A and C observation agree within 0.25° QD latitude with a standard deviation 0.47° and mean absolute deviation as small as 0.08°. This is a very convincing result.

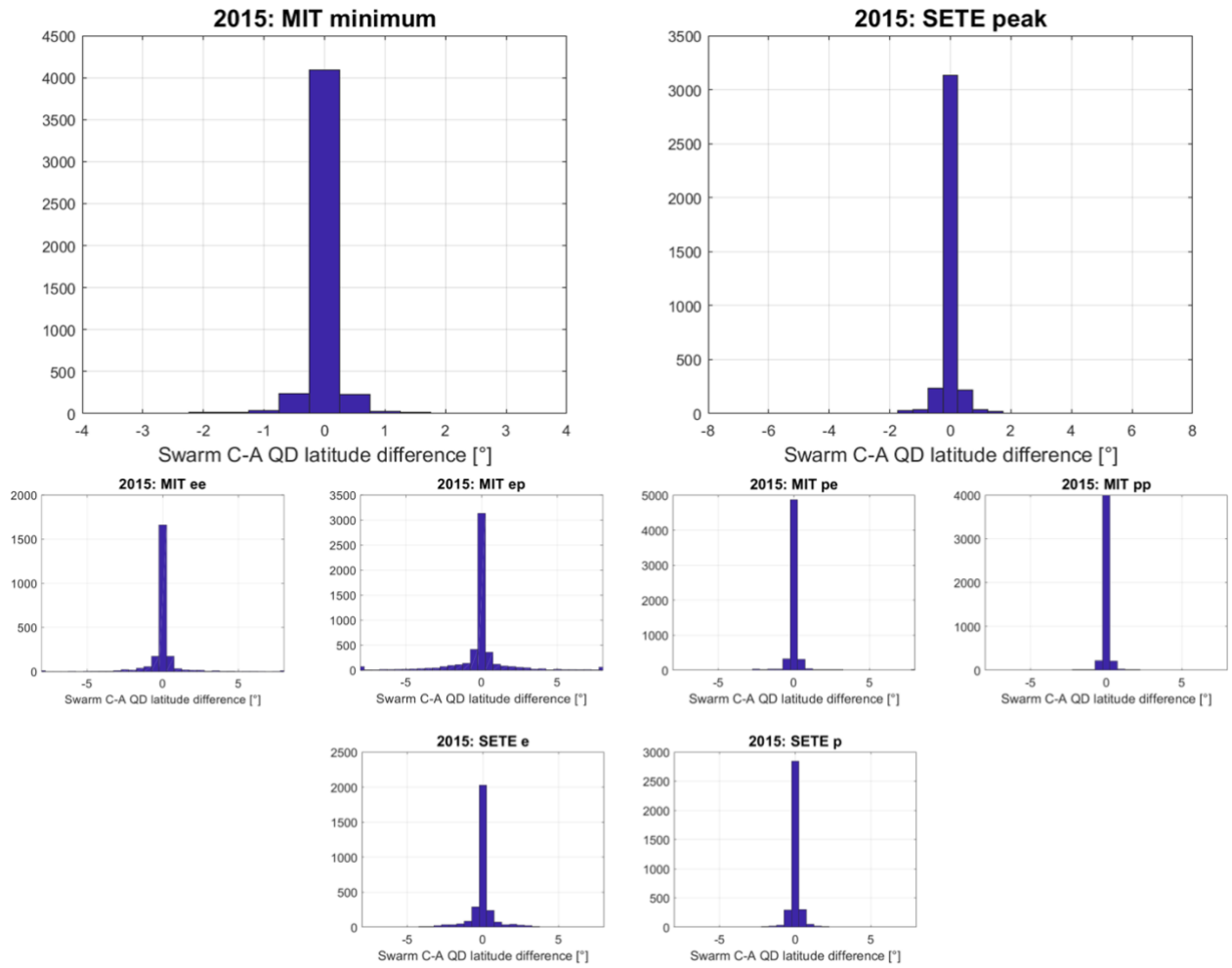


**Figure 4.4** Histogram of the differences of Swarm C and A observations of MIT minimum, SETE peak, MIT ee, MIT ep, MIT pe, MIT pp, SETE e, SETE p, respectively.

The second row of Figure 4.3 contains similar scatter plots for the EW edge (MIT_ee) and the PW edge (MIT_ep) of the EW MIT wall, as well as the EW edge (MIT_pe) and PW edge (MIT_pp) of the PW MIT wall,

respectively. Figure 4.4 presents the corresponding histograms. According to the plots, the PW wall can be established more safely and with higher accuracy than the EW wall. Especially the EW edge of the EW wall is difficult to locate in a significant part of the cases, because of the often gradual, smooth PW decrease of the density. Even so, in 89% of the observations of the EW edge of the EW wall the Swarm A-C difference is less than 1° QD latitude.

Finally, the bottom row in both Figure 4.3 and Figure 4.4 presents the results for the SETE boundaries. Again, the EW boundary (SETE_e) is found with less certainty. Here the difficulty is primarily related to the noise of the Te time series.

**Table 4-1** Standard deviation and median absolute deviation of the residuals of the differences between the Swarm A and C observations of the phenomena. Only observations with the highest quality flags are considered.

| | standard deviation | median abs. deviation |
|---|---|---|
| MIT pp | 0.83° | 0.09° |
| MIT pe | 1.16° | 0.09° |
| MIT minimum | 0.47° | 0.08° |
| MIT ep | 2.64° | 0.16° |
| MIT ee | 1.47° | 0.12° |
| SETE p | 0.63° | 0.10° |
| SETE peak | 0.46° | 0.09° |
| SETE e | 1.18° | 0.14° |

According to statistics, as well as the standard deviations of the differences listed in Table 4-1, the accuracy of the MIT detections can be estimated to around 0.5° for MIT, SETE, 1° for MIT pp, MIT pe, SETE_p and SETE_e boundaries, around 2° for MIT ee and MIT_ep. In general, it is often difficult to find the EW boundaries reliably. This is a very satisfying result for most of the boundaries except for the EW edge of both structures. This made the flagging of likely unreliable EW edge detections necessary.

### 4.1.3 Statistical validation

The dependence of the MIT location on MLT, as well as on the geomagnetic Kp index is well documented in the literature. The MLT dependence is characterised by a continuous decrease of the MIT latitude starting from the post-noon hours up to around sunrise. Afterwards the MIT moves quickly poleward. We checked these dependences in our data set (Swarm A, B and C, 2014-2020).

The result is plotted in Figure 4.5, separately for the two hemispheres. The expected feature clearly shows up in the data. Even though the number of detected cases decreases away from midnight, the expected trend is clear and is considered reliable.

The MIT location is also a function of geomagnetic activity. To check this, in Figure 4.6 we plotted the MIT location as function of MLT relative to midnight (horizontal axis) for different Kp ranges (colouring). In the MLT interval investigated, the MLT dependence can be modelled by a linear equation at any level of Kp. The parameters of the fit equations for both hemispheres are listed in Table 4-2.

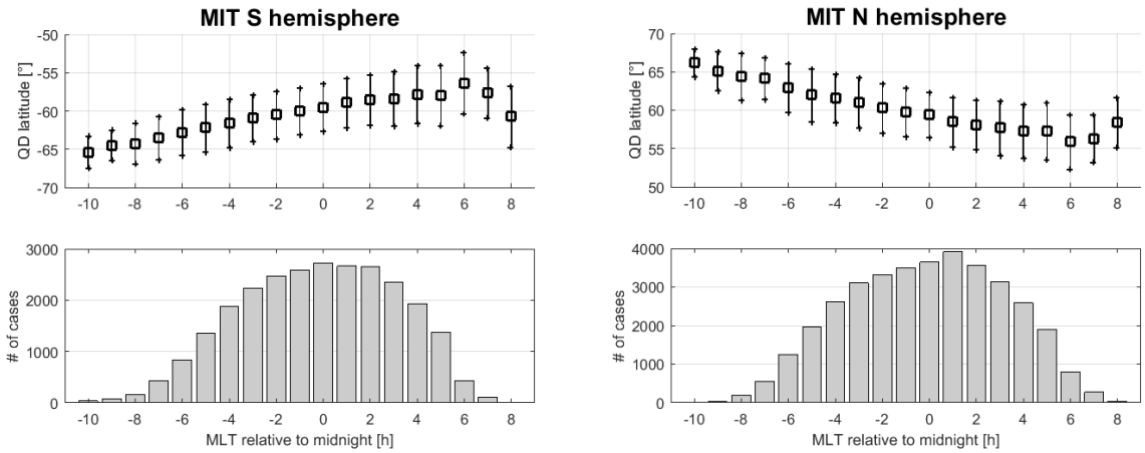


**Figure 4.5** MLT dependence of the MIT minimum location, separately for the northern (left) and southern (right) hemisphere. The bottom plots present the histograms of the occurrences.

The MIT moves around 2° EW as Kp increases by 1. The hourly EW shift of the MIT is typically between 0.6°¬0.8°. At low Kp, the EW movement is more pronounced in the N hemisphere. This asymmetry seems to diminish as Kp increases.

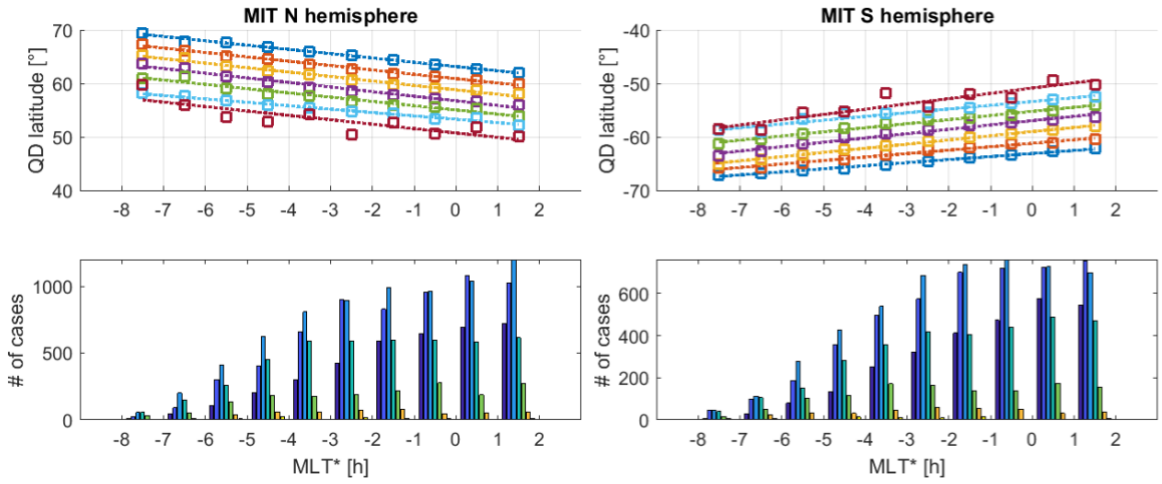


**Figure 4.6** MLT dependence of the MIT minimum at different level of geomagnetic activity (from top down-ward: Kp: 0-1, 1-2, 2-3, 3-4, 4-5, 5-6, 6-7), separately for the northern (left) and southern (right) hemisphere. The bottom plots present the histograms of the occurrences.

In the following, the distribution of the MIT wall locations and the locations of their inner and outer edges are presented (see Figure 4.7).

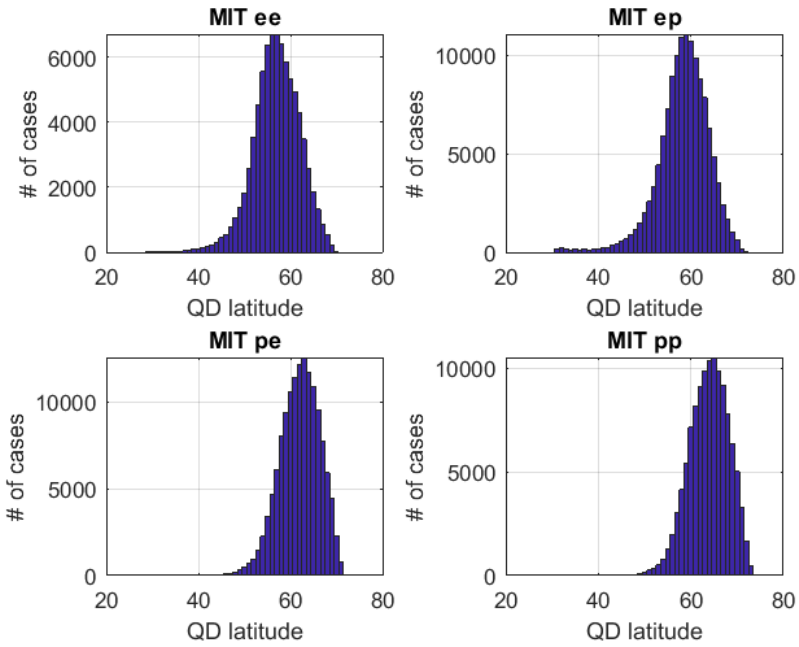


**Figure 4.7** Distribution of the MIT boundaries (top left) EW edge of the EW wall, (top right) PW edge of the EW wall, (bottom left) EW edge of the PW wall, (bottom right) PW edge of the PW wall.

The histogram of MIT ep, and especially MIT ee values have a pro-longed EW tail. This is likely caused, at least in part, by false detections of the EW edge included in the statistics. This may happen when the density decrease is smooth without significant changes in the gradient. MIT ep values below 40° occur very rarely, only during the most severe storms (which we do not have in our data sample). In such a rare case the MIT width is expected to be small. This issue is in part handled by boundary quality flags depending on QD latitude, MIT width and other parameters (for details see [AD-3]).

**Table 4-2** Parameters of the linear fits (MIT minimum location at midnight, slope of the fit) to the data points shown in Figure **4.6**. The 2nd and 3rd columns are for the N hemisphere, the 4th and 5th columns are parameters for the S hemisphere.

| Kp range | MIT qd_lat_0 [°] | Slope [°/h] | MIT qd_lat_0 [°] | Slope [°/h] |
|---|---|---|---|---|
| 0..1 | 63.15° N | -0.80 | 63.11° S | 0.57 |
| 1..2 | 60.89° N | -0.82 | 61.19° S | 0.65 |
| 2..3 | 58.80° N | -0.83 | 59.02° S | 0.78 |
| 3..4 | 56.75° N | -0.86 | 56.96° S | 0.81 |
| 4..5 | 55.05° N | -0.80 | 55.23° S | 0.77 |
| 5..6 | 53.29° N | -0.64 | 53.38° S | 0.70 |
| 6..7 | 50.73° N | -0.82 | 50.87° S | 0.99 |

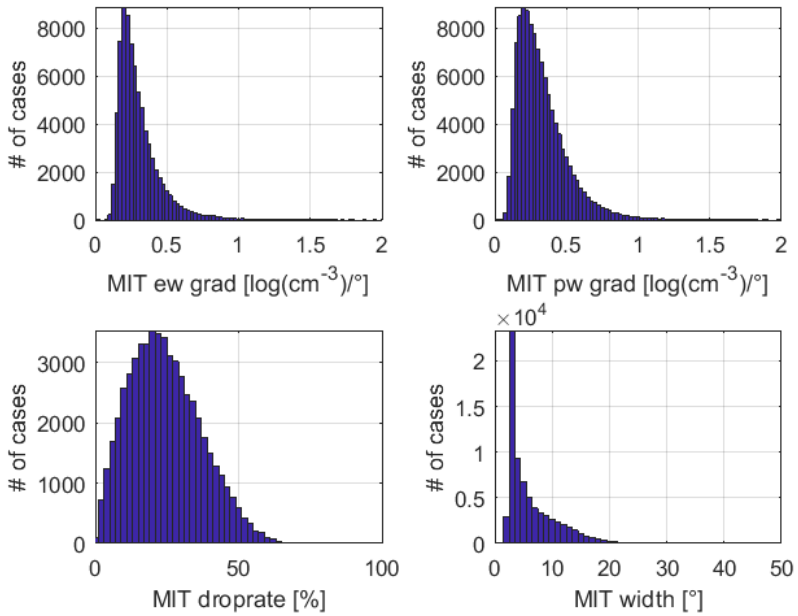


**Figure 4.8** (top left) EW wall gradient, (top right) PW wall gradient, (bottom left) MIT drop-rate, (bottom right) MIT width.

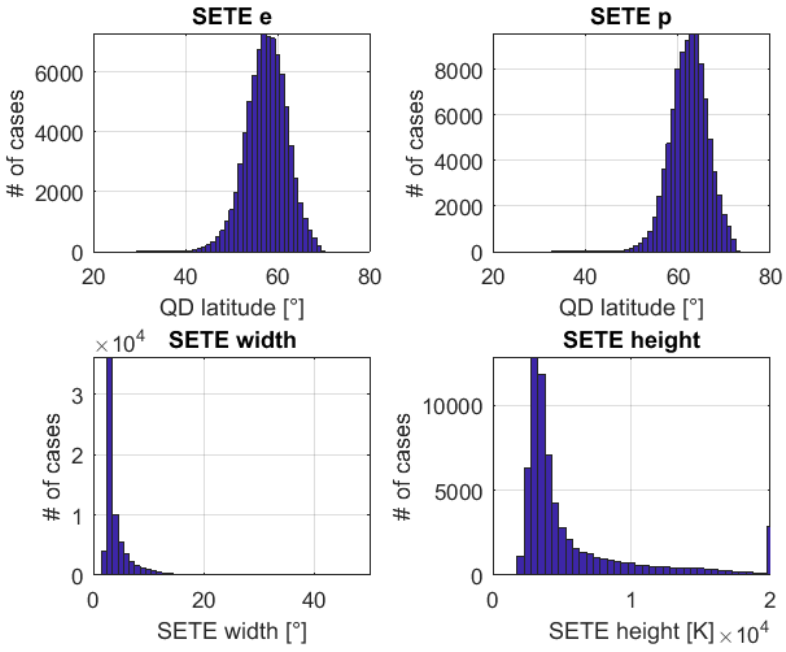


**Figure 4.9** SETE (top left) EW edge, (top right) PW edge, (bottom left) width, (bottom right) height.

In Figure 4.8 the wall gradients, the density drop rate within the MIT, and the MIT width are shown. In some of our case studies comparing the different PRISM products, it was found that even MIT records with density drop rate as low as 5% can provide the true MIT minimum positions. Nevertheless, in these cases, the wall definitions are considered uncertain. The MIT width is generally considered to vary between a few degrees

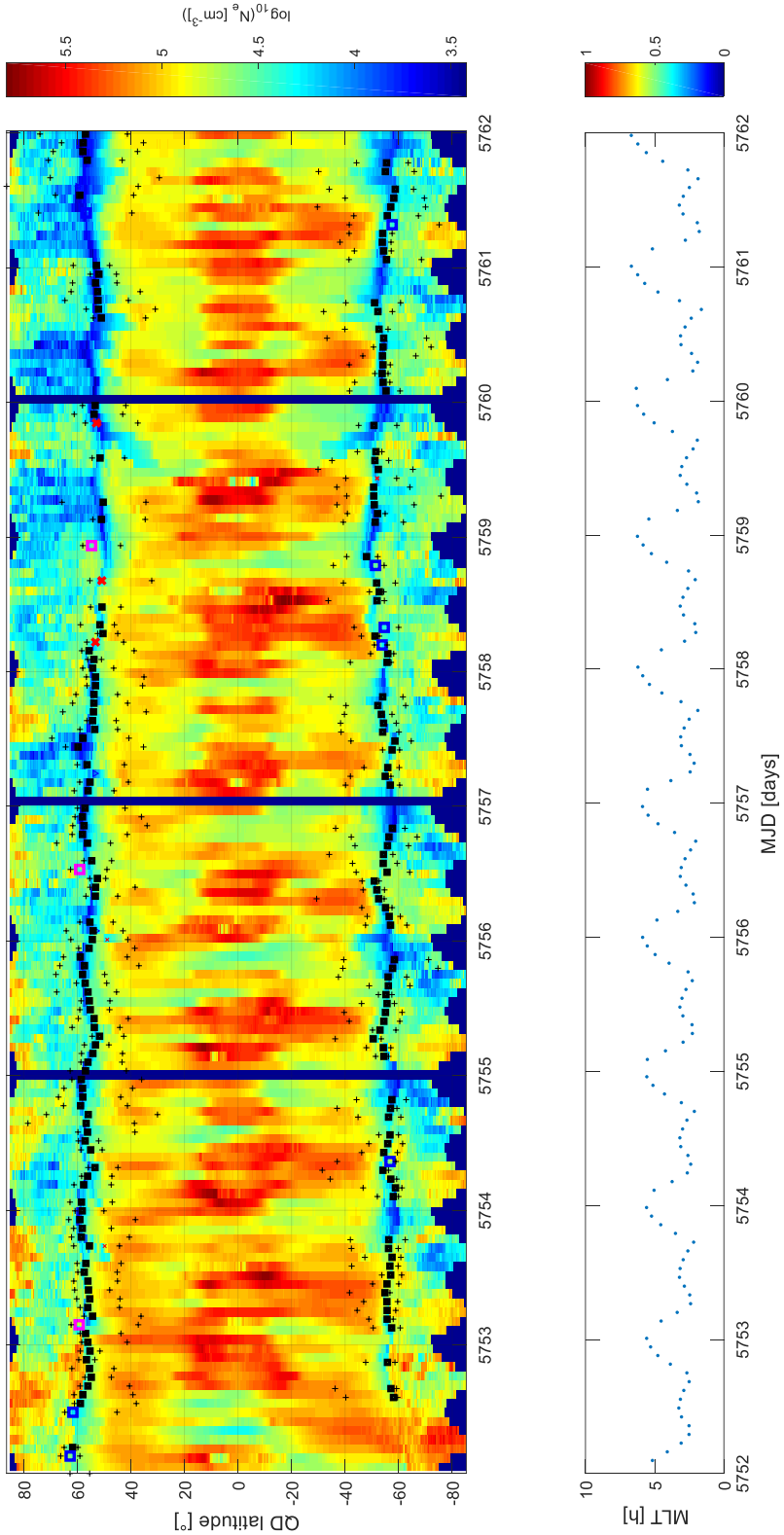


**Figure 4.10** (top) MITxTEC MIT minima (squares) and poleward and equatorward edges (black +) plotted over the LP log(Ne), (bottom) MLT at the equatorial crossing. Highest quality (main quality flag = 3) detections (minima) are shown in black, fair/poor quality (flagged by 2/1) are shown in blue/magenta, while likely false positives are crossed in red.

and around 20 degrees. This is consistent with previous investigations. Wider MITs typically are observed in the early morning hours.

The distribution of the EW and PW edges of SETE (Figure 4.9) is similar to the distributions of the corresponding MIT edges. The EW edge distribution has an elongated but narrow EW tail. Most of the detections forming this tail (below ~ 40° QD lat) are questionable detections and are flagged (see [AD-3]).

Despite the uncertainties, mostly related to the difficulties of the identification of the EW MIT edge, the behaviour of the MITx_LP product statistically agrees well with the expected, well-documented behaviour of the MIT.

## 4.2 MITxTEC_2F

### 4.2.1 Verification

In Figure 4.10 the MIT detections from the GPS TEC data are plotted over the log(Ne) maps. Compared to the MIT detection in LP Ne, the MIT detection in TEC is somewhat less efficient. In several cases, when the MIT is clearly found in the LP Ne, it is not clear in the TEC. This is because the TEC profiles are too smooth. This difference in behaviour is attributed to the fact, that TEC represents a column integrated density, and due to the spatial integration, the altitude-limited depletions are in part smoothed out. For the same reason, the detection of the MIT edges is even less straightforward. Nevertheless, the TEC data are still useful for monitoring the MIT minimum, as well as for confirming other observations and products. Especially on spacecraft not carrying a Langmuir probe but having a GNSS receiver on-board, as is the case for many operational LEO satellites, analysing GNSS TEC is still a valuable measure of to characterise the MIT.

### 4.2.2 Comparison between Swarm A and C

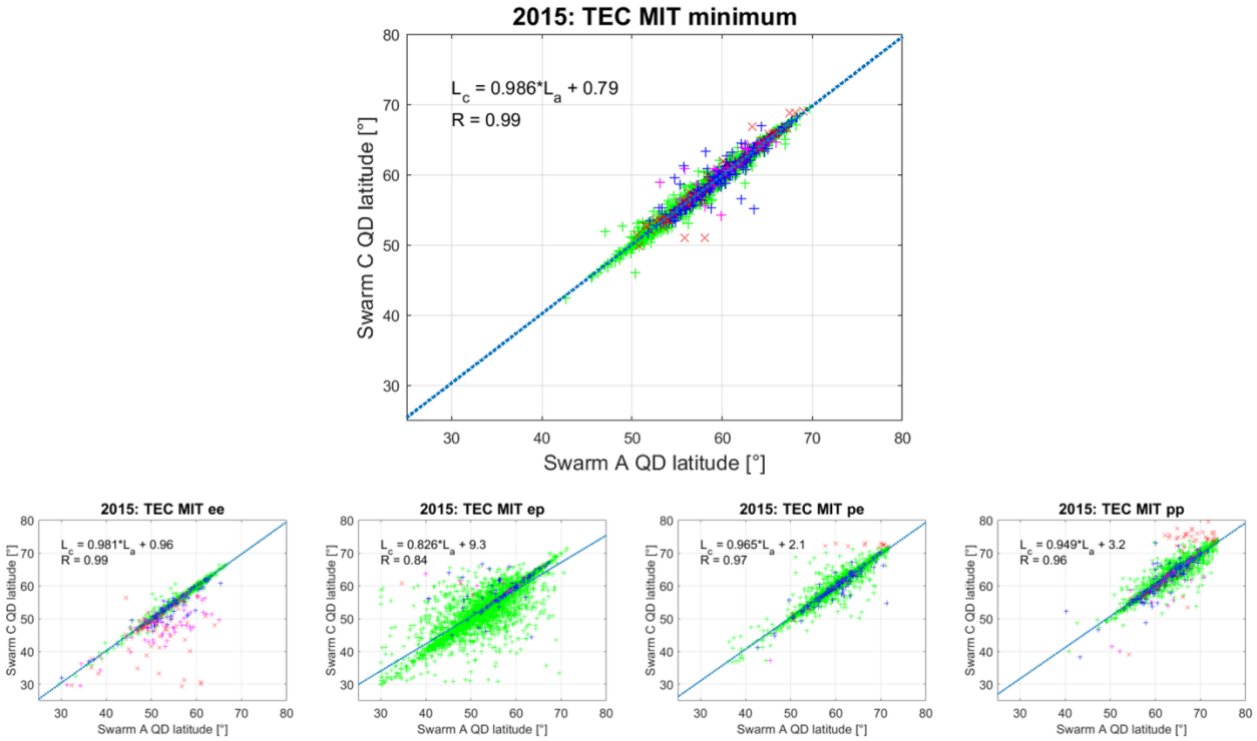


**Figure 4.11** (left) Same as Figure **4.3** first five subplots but derived from GPS TEC observations.

By comparing Swarm A and C observations, the accuracy of the TEC-derived MIT detections can be estimated in a similar way as for the LP-derived MIT detections (section 4.1.2). For the MIT minimum location, the detection accuracy is around 0.5°, while for the MIT wall edges it is around one degree, except for the PW edge of the EW wall that is a few degrees.

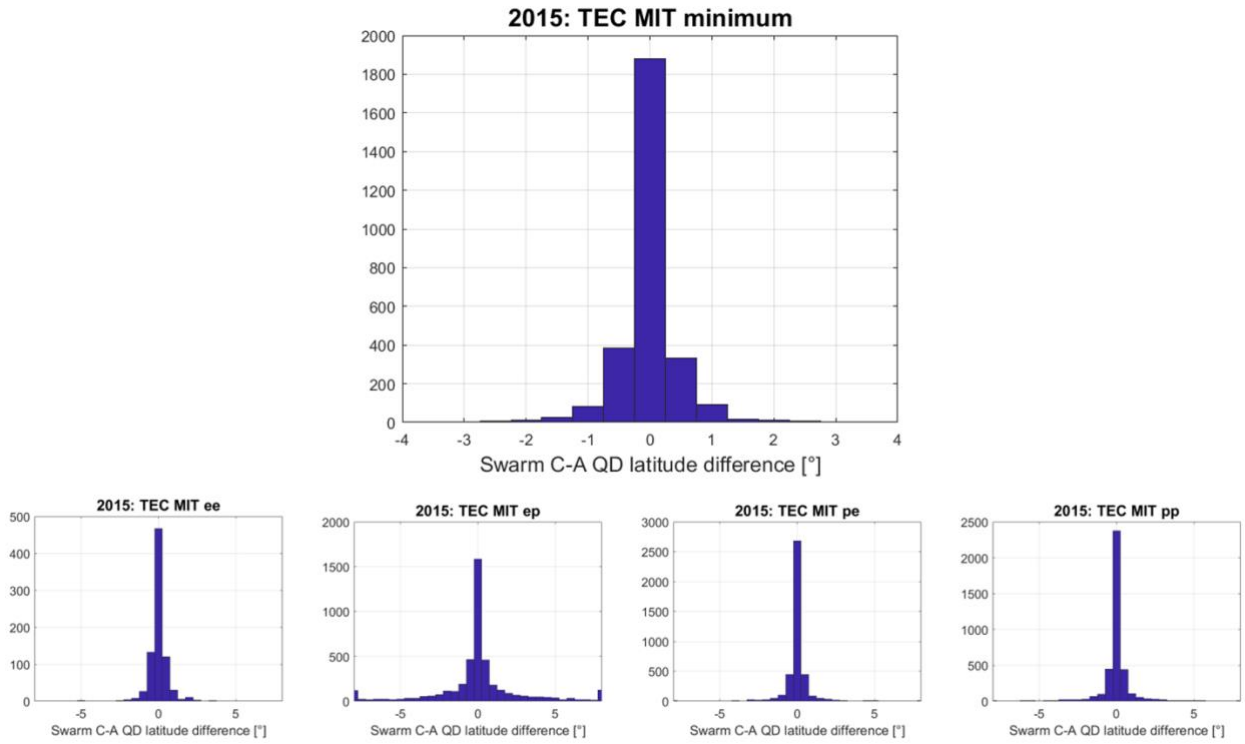


**Figure 4.12** (left) Same as Figure **4.4** first five subplots but derived from GPS TEC observations.

**Table 4-3** Standard deviation and median absolute deviation of the residuals of the differences between the Swarm A and C observations of the phenomena.

| | standard deviation | median abs. deviation |
|---|---|---|
| MIT pp | 1.23° | 0.17° |
| MIT pe | 1.21° | 0.15° |
| MIT minimum | 0.49° | 0.15° |
| MIT ep | 3.71° | 0.20° |
| MIT ee | 0.73° | 0.20° |

As a consequence, the MIT as derived from GPS (GNSS) TEC observations is less suitable for the study of the MIT structure, however, this product has a great potential in monitoring the MIT minimum.

### 4.2.3 Statistical validation

The MLT and Kp dependence of the MIT position reflected in the TEC-derived product (all three Swarm satellites, 2014-2020) is presented in Figure 4.13, and the parameters of the linear fit models of the MLT dependence at different level of Kp are given in Table 4-4. The MITxTEC product, similarly to the MIT_xLP version, clearly shows the expected behaviour.

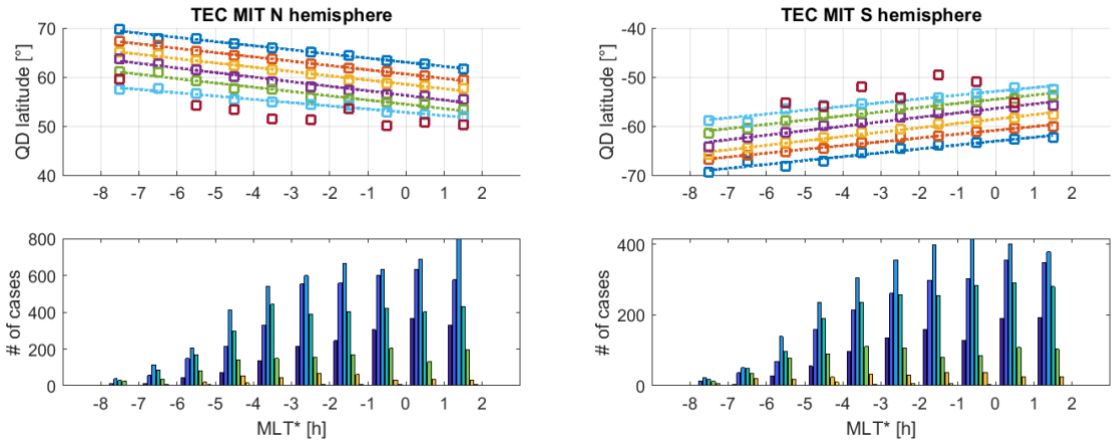


**Figure 4.13** MLT dependence of the MIT minimum at different level of geomagnetic activity (equatorward: Kp: 0-1, 1-2, 2-3, 3-4, 4-5, 5-6, 6-7), separately for the northern (left) and southern (right) hemisphere. The bottom plots present the histograms of the occurrences.

**Table 4-4** Parameters of the linear fits (MIT minimum location at midnight, slope of the fit) to the data points shown in Figure **4.13**. The 2nd and 3rd columns are for the N hemisphere, the 4th and 5th columns are parameters for the S hemisphere.

| Kp range | MIT qd_lat_0 [°] | Slope [°/h] | MIT qd_lat_0 [°] | slope °/h] |
|---|---|---|---|---|
| 0..1 | 63.01° N | -0.85 | 63.08° S | 0.79 |
| 1..2 | 60.60° N | -0.87 | 60.87° S | 0.78 |
| 2..3 | 58.50° N | -0.88 | 58.57° S | 0.89 |
| 3..4 | 56.25° N | -0.93 | 56.41° S | 0.91 |
| 4..5 | 54.43° N | -0.88 | 54.53° S | 0.85 |
| 5..6 | 52.79° N | -0.67 | 52.93° S | 0.77 |

The analysis of the MIT walls derived from TEC points again at the difficulty of the EW edge detection. TEC profiles are even smoother than LP Ne profiles, and the EW edge of the EW wall can be determined reliably only in the minority of the MIT detections (Figure 4.14). The EW edge is uncertain whenever the MIT width exceeds around 10°-15°.

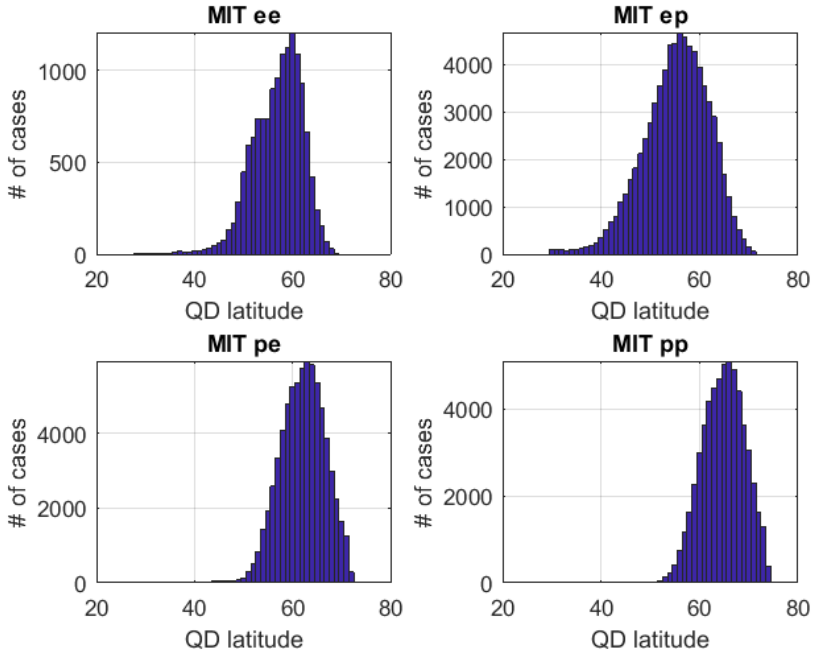


**Figure 4.14** Distribution of the MIT boundaries (top left) EW edge of the EW wall, (top right) PW edge of the EW wall, (bottom left) EW edge of the PW wall, (bottom right) PW edge of the PW wall derived from TEC observations.

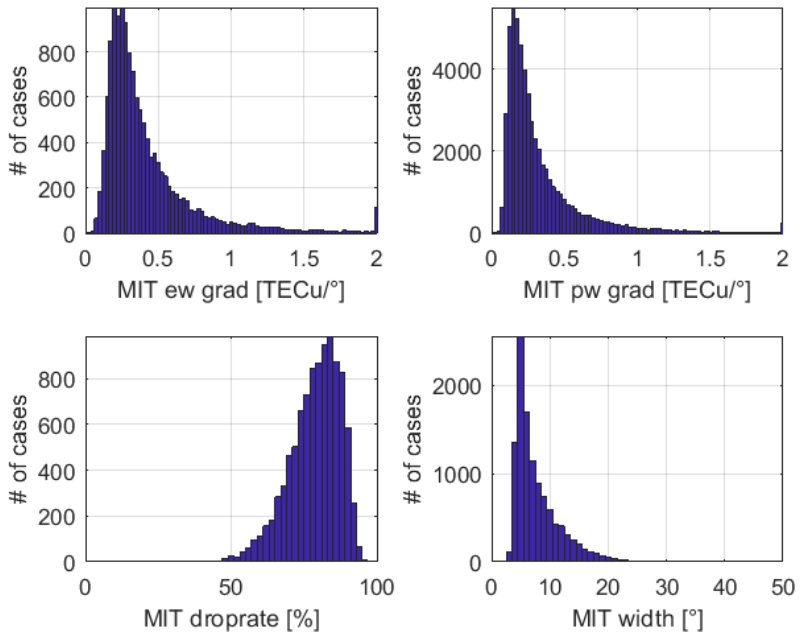


**Figure 4.15** (top left) EW wall gradient, (top right) PW wall gradient, (bottom left) MIT drop-rate, (bottom right) MIT width derived from TEC data.

In the following, in Figure 4.15 the statistics of the wall gradients, TEC drop rates and MIT width are presented. Note, that for the drop rate calculation a 2 TECU offset is added to all observed TEC values to avoid negative TECs and division by close-to-zero values. The most frequent MIT width is around 5°, and the MIT is hardly ever wider than 20°. This is consistent with previous findings.

The analysed events show the expected behaviour of the MIT.

## 4.3 PPIxFAC_2F

### 4.3.1 Verification

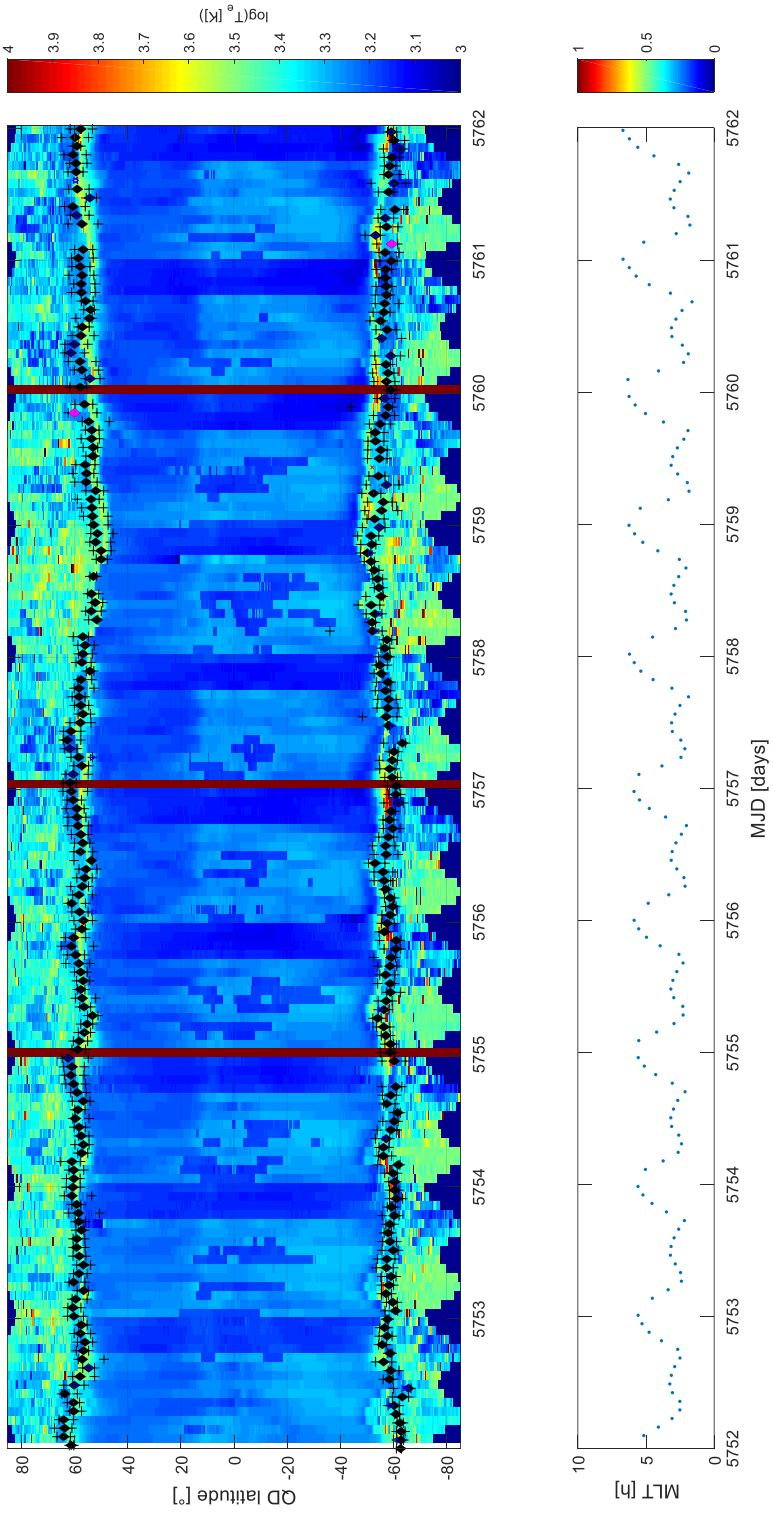


**Figure 4.16** (top) PPIxFAC SSFAC boundary (diamonds) and poleward and equatorward boundaries (black +) plot-ted over the LP log(Te), (bottom) MLT at the equatorial crossing. Highest quality (main quality flag = 3) detections (minima) are shown in black, fair/poor quality (flagged by 2/1) are shown in blue/magenta, while likely false positives are crossed in red.

In Figure 4.16 the SSFAC boundary is plotted over a 2D Ne as a verification of the efficiency of the boundary detection. The same ten-day interval around autumn equinox (1-10 Oct, 2015) was chosen, as for the other pruducts.

### 4.3.2 Comparison between Swarm A and C

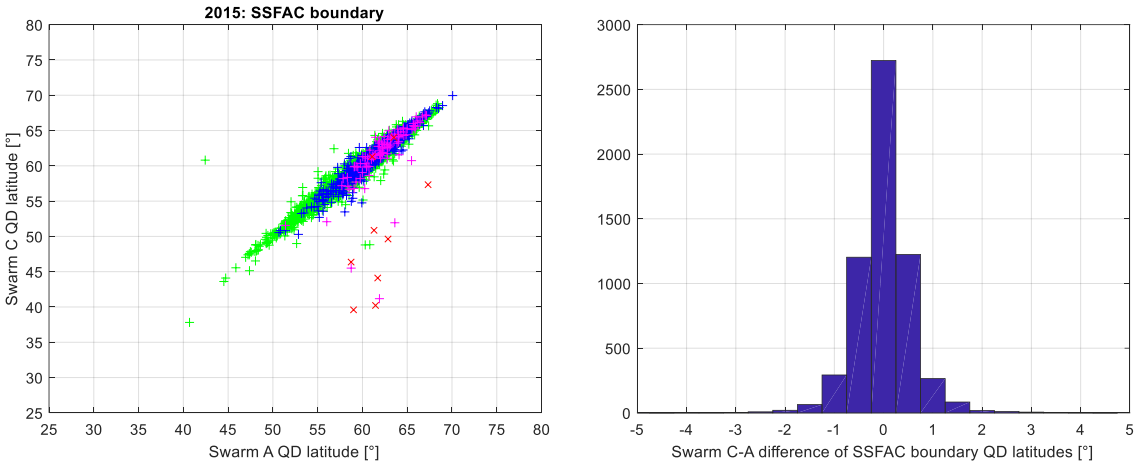


**Figure 4.17** (left) Same as Figure **4.3** first subplot but for SSFAC boundary observations. (right) Same as Figure **4.4** first subplot but derived from Figure **4.17** left plot.

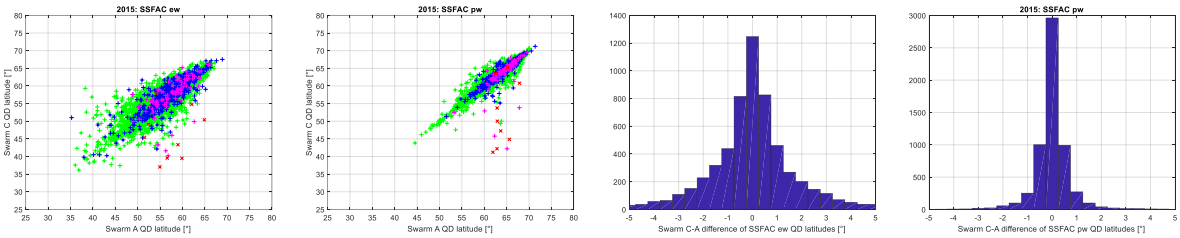


**Figure 4.18** Same as Figure **4.17** but for the EW and PW edge of the SSFAC boundary.

**Table 4-5** Standard deviation and median absolute deviation of the residuals of the differences between the Swarm A and C observations of the phenomena.

| | standard deviation | median abs. deviation |
|---|---|---|
| SSFAC pw | 0.84° | 0.25° |
| SSFAC boundary | 0.65° | 0.28° |
| SSFAC ew | 2.13° | 0.78° |

### 4.3.3 Statistical validation

The SSFAC boundary also very sensitively reacts to any change in geomagnetic activity, however, it does not show the strong MLT dependence that MIT does. Instead, as found by [RD-1] and [RD-2], at any given level of Kp, the boundary follows a circle on an MLT dial plot (in L-space). This representation corresponds to an

equatorial cut of the magnetosphere. To derive Figure 4.19, all data from the beginning of the Swarm mission until the end of 2019, as well as CHAMP data recorded between 2001 and 2008 were used, i.e., altogether 161137 boundary crossings.

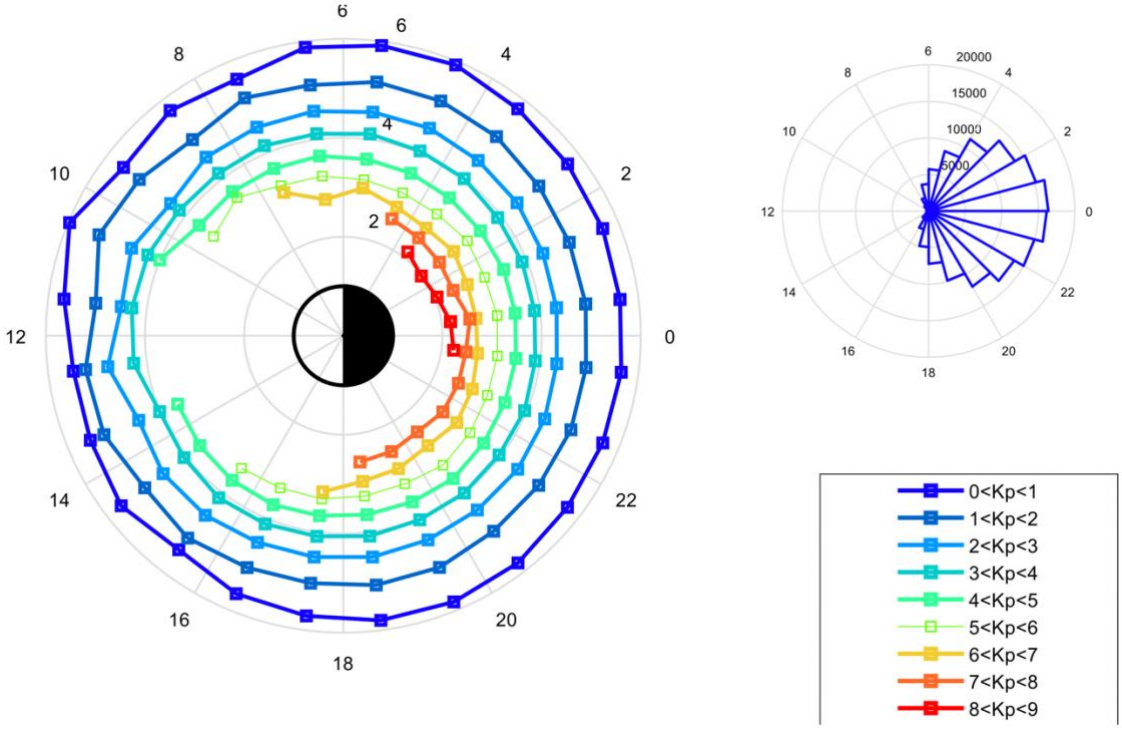


**Figure 4.19** (left) MLT dial plot of the SSFAC boundaries observed by CHAMP and Swarm at different level of Kp, (right) MLT distribution of the boundary observations.

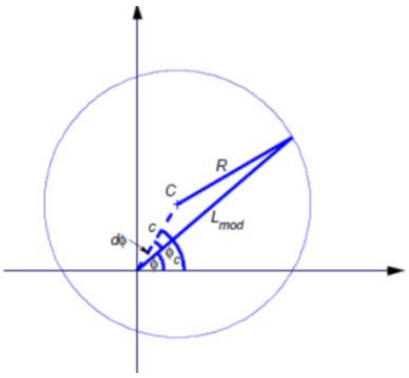


**Figure 4.20** Sketch of the SSFAC boundary model.

The simple geometry of the boundary allows us to fit a simple model (Figure 4.20): ex-centric circles with Kp-dependent radius. The model can be formulated as:

$$L_{model} = c \cdot \cos d\varphi + \sqrt{R^2 - c^2 \sin^2 d\varphi}\,, \qquad \text{Eq. 4.3-1}$$

where $d\varphi = 2\pi\big((\mathrm{MLT} - \mathrm{MLT_c})/24\big)$, and $\mathrm{MLT_c} = \varphi_c \cdot 24\mathrm{h}/360^\circ$, $R = R_0 + p_1\mathrm{Kp} + p_2\mathrm{Kp}^2$, $c = c_0 + \gamma_c\mathrm{Kp}$, $\mathrm{MLT}_\gamma = \mathrm{MLT}_0 + \gamma_{mlt}\mathrm{Kp}$.

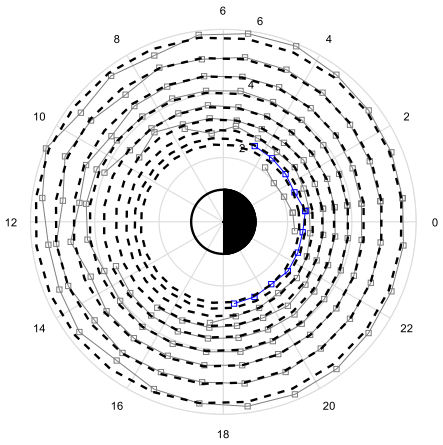


**Figure 4.21** The model fitted to the observational data.

To achieve a good fit also for poorly represented higher Kp values, a weighted least squares regression was applied with Kp indices as weights. The resulting model (Figure 4.21) coefficients and their 95% confidence intervals are given in Table 4-6.

**Table 4-6** SSFAC boundary model coefficients.

| | | | 95% confidence interval | | |
|---|---|---|---|---|---|
| nr | Parameter | Value | lower bound | upper bound | Unit |
| 1 | $R_0$ | 6.06 | 6.05 | 6.08 | $R_E$ |
| 2 | $p_1$ | - 0.684 | - 0.691 | - 0.678 | $R_E$ |
| 3 | $p_2$ | 0.0309 | 0.0300 | 0.0318 | $R_E$ |
| 4 | $c_0$ | 0.15 | 0.14 | 0.17 | $R_E$ |
| 5 | $\gamma_c$ | 0.005 | 0.000 | 0.009 | $R_E$ |
| 6 | $MLT_0$ | 10.69 | 10.48 | 10.90 | h |
| 7 | $\gamma_{mlt}$ | 0.402 | 0.340 | 0.463 | h |

The first three parameters describe the Kp-dependent equatorial radius. The saturated PP has a radius of around 6.06 RE. The PP moves inward by 0.00, -0.65, -1.24, -1.77, -2.24, -2.65, -2.99, -3.27, -3.49, -3.65 RE, as a response to Kp increase from 0 to 9. Parameters four to eight describe the location of the centre of the circles and its dependence on Kp. At quiet conditions, the centre stands at 0.15 RE toward ~11 MLT with respect to the centre of the Earth. The distance from the Earth centre hardly changes with Kp (it is ~0.20 RE at Kp = 9), and it moves toward dusk by increasing geomagnetic activity. This is probably related to the movement of the dusk side bulge of the plasmasphere.

This model is applied for the derivation of the PPI index as described in [AD-3]. The model is used to calculate the SSFAC boundary position at midnight from the boundary position observed at any MLT. During this calculation, c0 is taken 0.15, and the radius of the boundary is calculated from the actual observations.

## 4.4 Comparison of the PRISM products

The three PRISM products were also compared to each other. Figure 4.22 presents the Swarm A observations of four boundaries for a 20-day interval starting on 1 Jan, 2015. In each subplot, all the four boundaries are shown, however, in each subplot a different boundary is highlighted by using darker and greater symbols. In the four panels from top downward the SSFAC boundary (diamonds), the MIT Ne minimum (downward triangles), the SETE peak (upward triangles), and the MIT TEC minimum (circles) are highlighted. The four boundaries, despite the differences in the details (e.g., the opening gap between SSFAC boundary and the other boundaries following a sudden drop-in geomagnetic activity, such as in day 5485) of their evolution, follow very similar trends. This is because of their common sensitivity to the variations of geomagnetic activity.

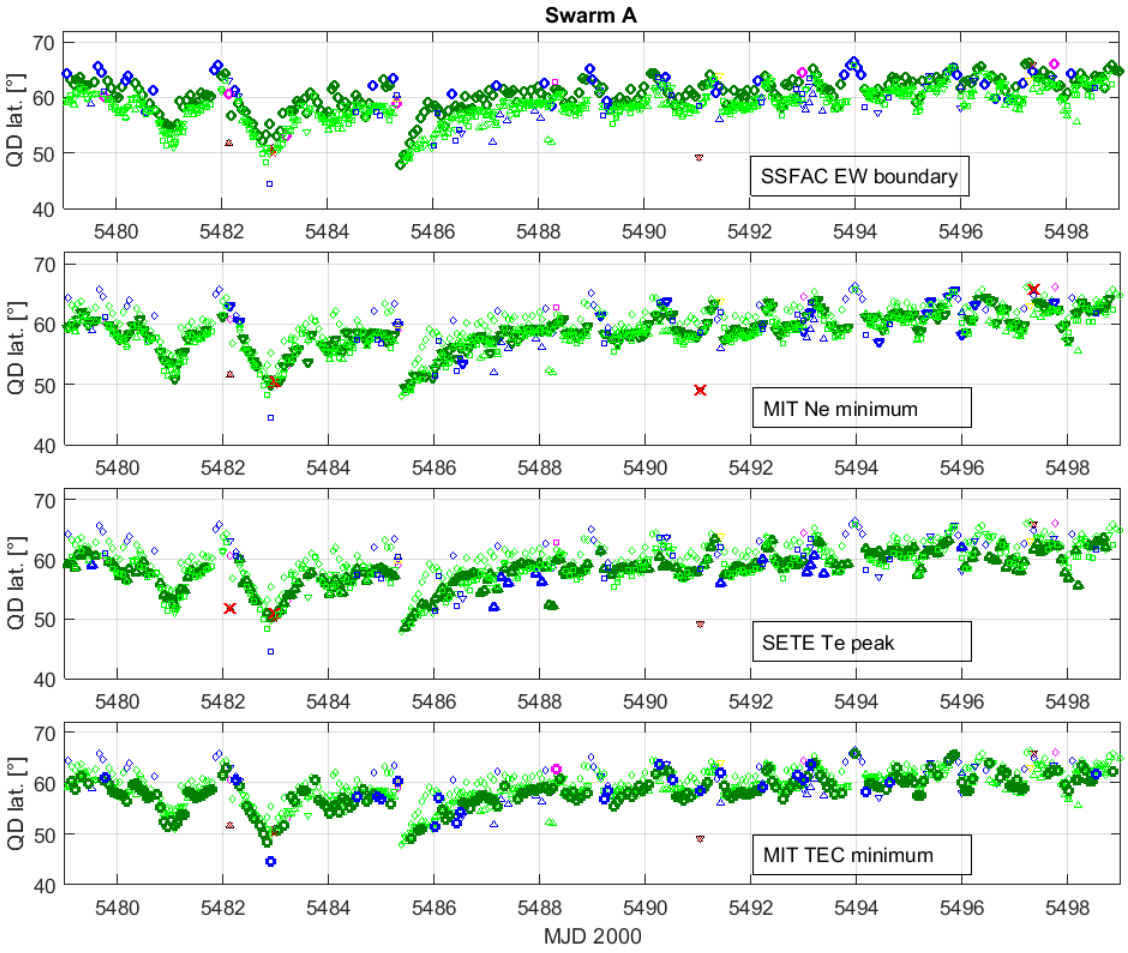


**Figure 4.22** Swarm A observations of the locations of (from top to bottom) the SSFAC boundary, the MIT Ne minimum, SETE peak, and the MIT TEC minimum between 1 and 20 Jan, 2015. In each subplot all the four boundaries are shown, however, one of them is enhanced (by darker, greater and thicker symbols). Colouring is according to the quality indicator as in previous plots.

In the following, the results of the statistical comparison of these boundaries are presented as L-differences versus MLT (MLT relative to midnight). These comparisons are all based on Swarm A and B observations made in 2015 and 2017. All observations regardless to their quality were considered. For each comparison, first a scatter plot of their difference vs. MLT is presented. Then a linear trend is fitted, and the resulting fit equation is given. Finally, the histogram of the de-trended difference (residuals after fit removed) is plotted, and the vector QQ of the [0.025 0.10 0.25 0.75 0.90 0.975] quantiles calculated from the de-trended differences is given. Similar statistical calculations are the base for the definition of a series of quality flags.

### 4.4.1 MITx_LP MIT minimum and PPxFAC SSFAC boundary

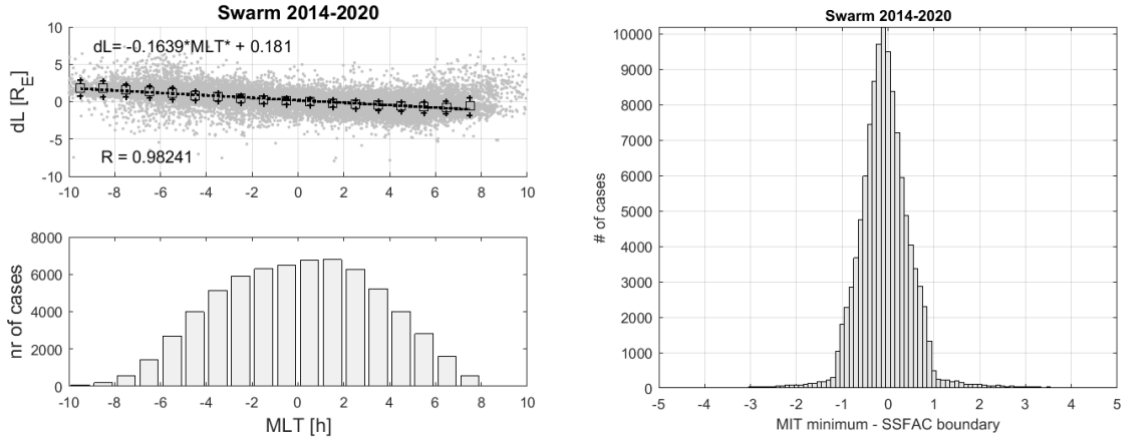


**Figure 4.23** (left) L-difference of the MIT Ne minimum and the SSFAC boundary as a function of MLT relative to midnight, (right) Histogram of the residuals of the L-difference after the linear MLT dependence is eliminated.

$$dL_{MITxLP-PPIxFAC} = -0.164 \cdot MLT^{*} + 0.18 \qquad \text{Eq. 4.4-1}$$

$$QQ = [-1.07 \ -0.71 \ -0.40 \ 0.08 \ 0.60 \ 0.98$$

where $MLT^{*} = (\mathrm{mod}(MLT + 12{,}24) - 12)$, i.e., MLT relative to midnight. The median of the residuals is close to zero. The two boundaries cross each other in the post-midnight sector (at MLT = 1:26). The difference does not depend on Kp (not shown), i.e., the boundaries move together responding geomagnetic activity variations, they seem dynamically coupled.

### 4.4.2 MITx_LP MIT minimum and MITx_LP SETE peak

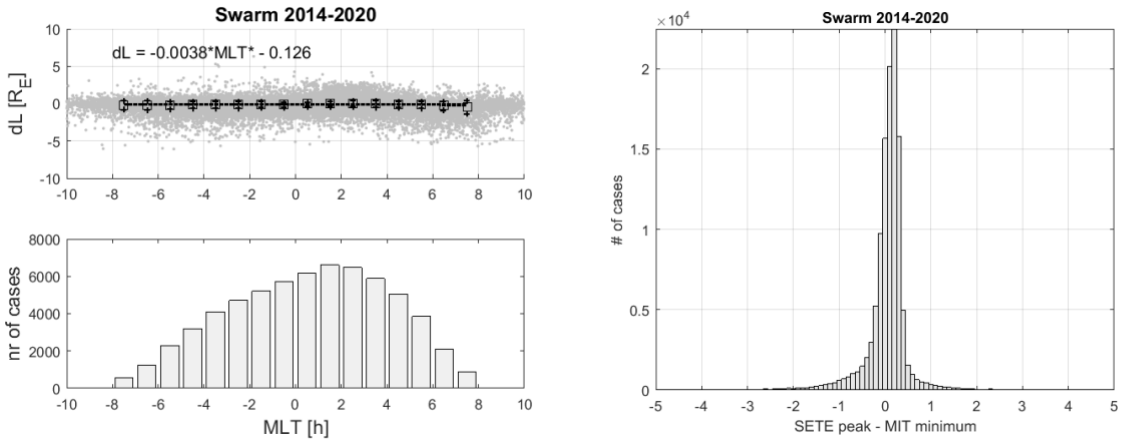


**Figure 4.24** (left) L-difference of the MIT Ne minimum and the SETE peak as a function of MLT relative to mid-night, (right) Histogram of the residuals of the L-difference after the linear MLT dependence is eliminated.

$$dL_{SETE-MITxLP} = -0.004 \cdot MLT^* - 0.13 \qquad \text{Eq. 4.4-2}$$

$$QQ = [-1.13 \ -0.33 \ -0.05 \ 0.24 \ 0.35 \ 0.78]$$

### 4.4.3 PPIxFAC SSFAC boundary and MITx_LP SETE peak

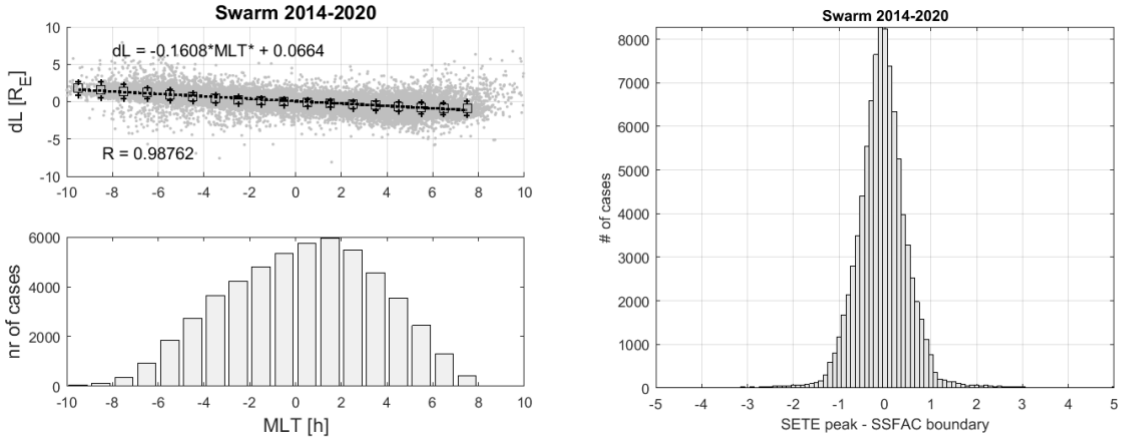


**Figure 4.25** (left) L-difference of the SETE peak and the SSFAC boundary as a function of MLT relative to midnight, (right) Histogram of the residuals of the L-difference after the linear MLT dependence is eliminated.

$$dL_{SETE-PPIxFAC} = -0.161 \cdot MLT^* + 0.07 \qquad \text{Eq. 4.4-3}$$

$$QQ = [-1.12 \ -0.70 \ -0.37 \ 0.24 \ 0.58 \ 1.00]$$

### 4.4.4 MITxTEC MIT minimum and PPxFAC SSFAC boundary

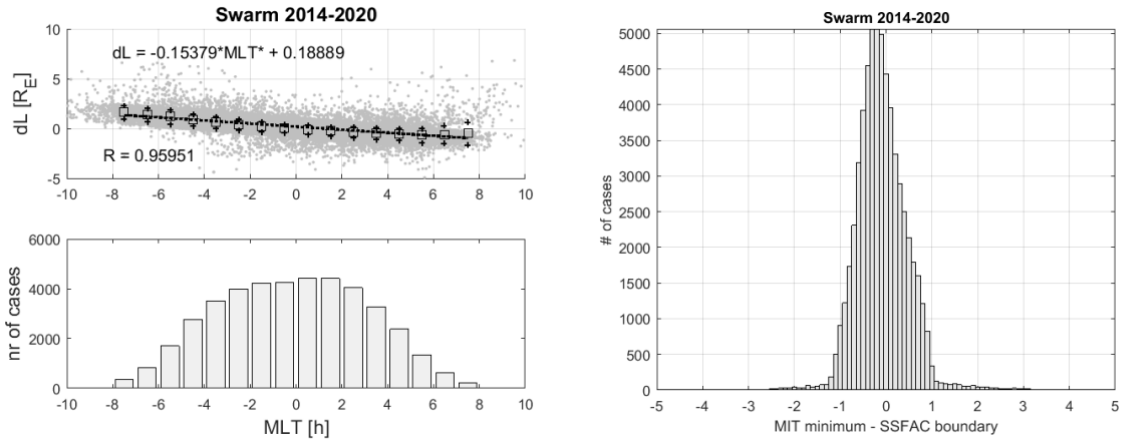


**Figure 4.26** (left) L-difference of the MIT TEC minimum and the SSFAC boundary as a function of MLT relative to midnight, (right) Histogram of the residuals of the L-difference after the linear MLT dependence is eliminated.

$$dL_{MITxTEC-PPIxFAC} = -0.154 \cdot MLT^* + 0.19 \qquad \text{Eq. 4.4-4}$$

$$QQ = [-1.03 \ -0.73 \ -0.44 \ 0.22 \ 0.62 \ 0.95]$$

### 4.4.5 MITx_LP MIT minimum MITxTEC MIT minimum

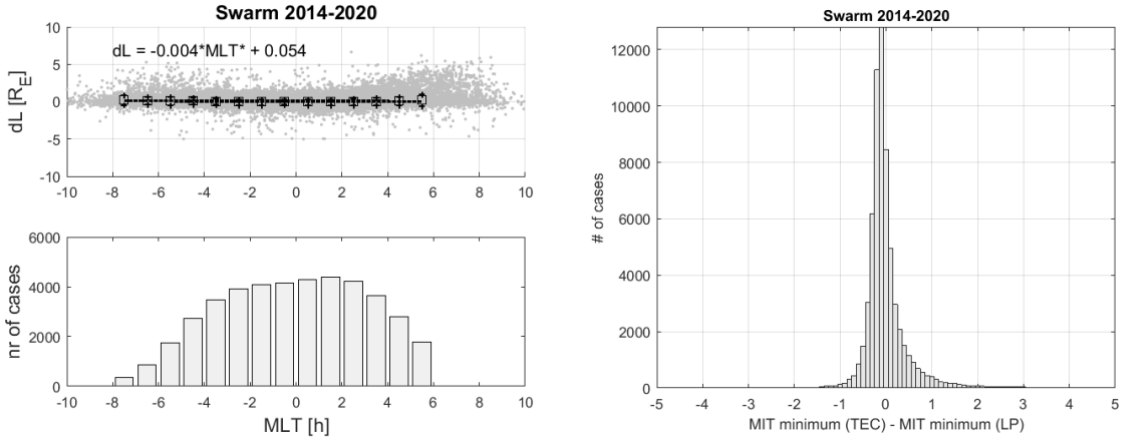


**Figure 4.27** (left) L-difference of the MIT Ne and MIT TEC minima as a function of MLT relative to midnight, (right) Histogram of the residuals of the L-difference after the linear MLT dependence is eliminated.

$$dL_{MITxTEC-MITxLP} = -0.004 \cdot MLT^* + 0.05 \qquad \text{Eq. 4.4-5}$$

$$QQ = [-0.65 - 0.36 \ -0.22 \ 0.08 \ 0.45 \ 1.29]$$

### 4.4.6 MITxTEC MIT minimum MITx_LP SETE peak

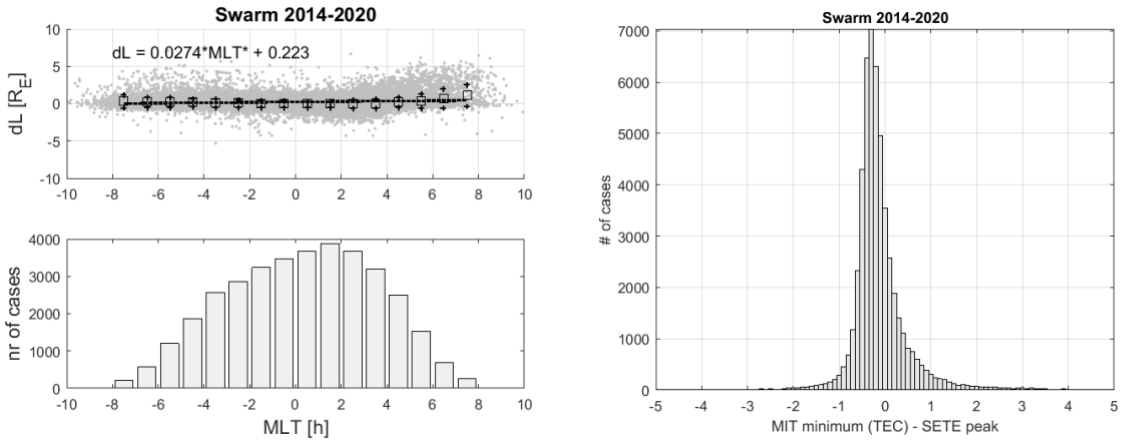


**Figure 4.28** (left) L-difference of the MIT TEC minimum and the SETE peak as a function of MLT relative to mid-night, (right) Histogram of the residuals of the L-difference after the linear MLT dependence is eliminated.

$$dL_{MITxTEC-SETE} = 0.027 \cdot MLT^{*} + 0.22 \qquad \text{Eq. 4.4-6}$$

$$QQ = [-1.00 \ -0.58 \ -0.41 \ -0.04 \ 0.49 \ 1.46]$$

### 4.4.7 Summary of product comparisons

Both the MIT minimum (derived either from LP or TEC) as well as SETE peak show an MLT dependence in their location as was already shown in 4.1.3 and 4.2.3, while the same behaviour is not present in the SSFAC boundary. This difference in the boundary characteristics appear also in all comparisons between the MIT/SETE boundaries with the SSFAC boundary.

The difference between the MIT minima deduced from LP and TEC observations is smaller than dL = 0.5 (maps into a latitude dependent QD latitude uncertainty, e.g., 5.8°/1.9°/0.3° at 45°/60°/75° QD latitudes, respectively) in 80% of all cases. The distance between the SETE peak and of the LP/TEC variant of the MIT minimum is also small, typically below 0.4/0.7 (5-7°/2-3°/0.2-0.3° uncertainty at 45°/60°/75° QD latitudes). All these results are in agreement with the expectations for the products.

# 5 Validation by independent data sets

A validation of the product should involve independent data. To validate the potential use of the PRISM products in monitoring plasmaspheric dynamics these validating data should come from plasmaspheric observations. Fortunately, there have been quite a number of (otherwise rare) plasmaspheric missions in the recent years. The two RBSP (Van Allen Probes) of NASA were launched in 2012 and operated until 2020, providing near-equatorial in-situ electron density data up to L = 5.8 (see Figure 5.1). The similar Japanese ERG (Arase) was launched at the end of 2016 and yields density data up to L = 6. The longest dataset covering the wider L-range comes from the NASA THEMIS mission. In the interval of interest THEMIS A, D and E covered the L = 1.1-16 range.

Unfortunately, the THEMIS spacecraft do not observe the cold (~ 1 eV) density. As shown below based on the spacecraft potential a density proxy can be derived that is sufficient for PP detection.

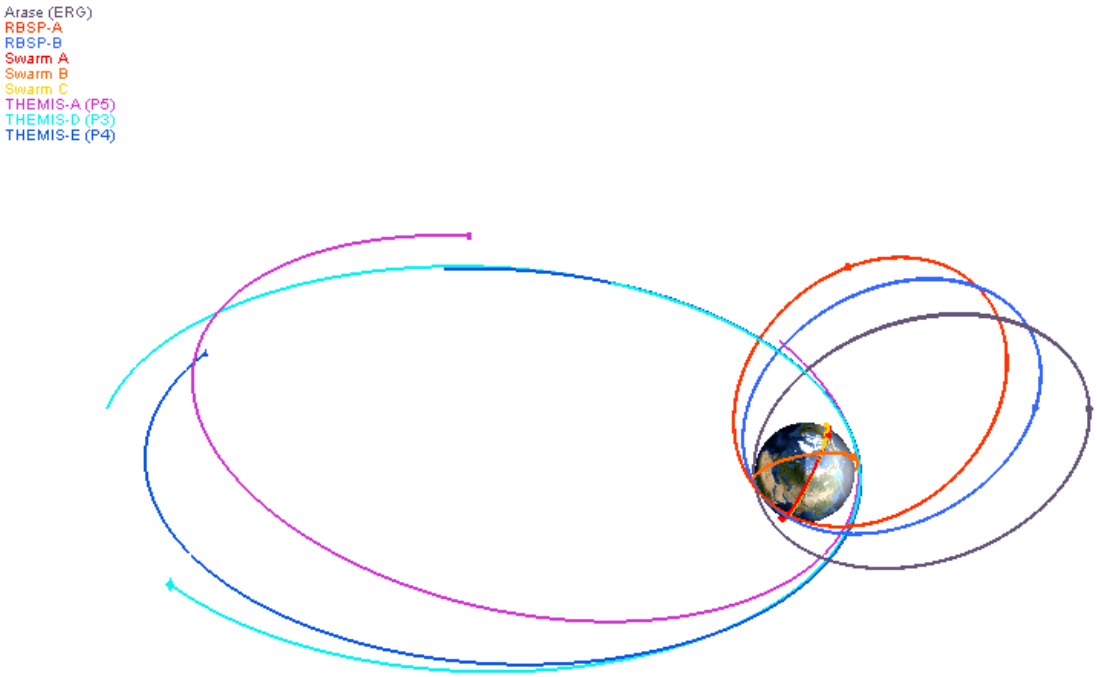


**Figure 5.1** An illustration of the orbits of the satellites yielding the validating data set.

Following [RD-3] and [RD-4], we estimate THEMIS electron number density $N_{pot}$ from the spacecraft potential $\varphi_{s/c}$ using a formula

$$N_{pot} = ae^{-\frac{\varphi}{b}} + ce^{-\frac{\varphi}{d}} \qquad \text{Eq. 5-1}$$

where the potential $\varphi = \varphi_{s/c} + \varphi_{bias}$, and $\varphi_{bias}$ is a constant bias potential, in this case 2V, while *a*, *b*, *c*, and *d* are model parameters found by fitting the model to observational data and/or a plasmaspheric model. For the calibration of the data outside the plasmasphere we used THEMIS ESA (electrostatic analyser) density measurements. ESA density includes only the suprathermal (from a few eV to 30 keV) electrons. $N_{pot} \approx N_{esa}$ only during strong convection, otherwise $N_{pot} > N_{esa}$ (see e.g., Figure 5.2).

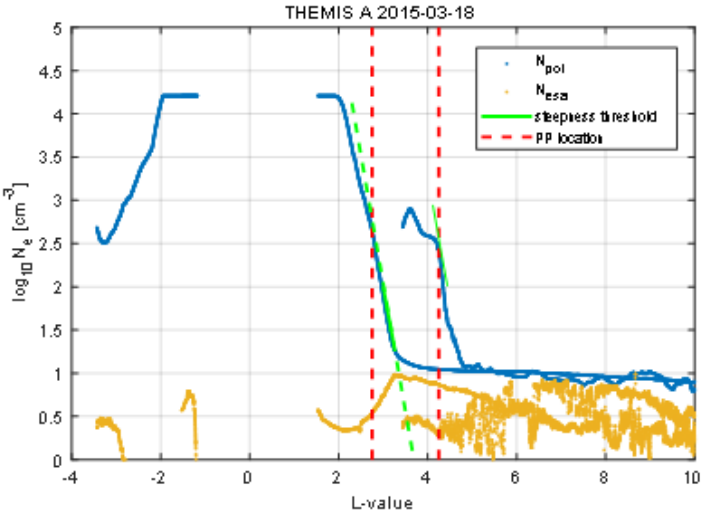


**Figure 5.2** An example of the THEMIS density proxy (blue solid line) compared to the ESA density (yellow line). Dashed green/red lines represent the applied threshold steepness/the PP location, respectively.

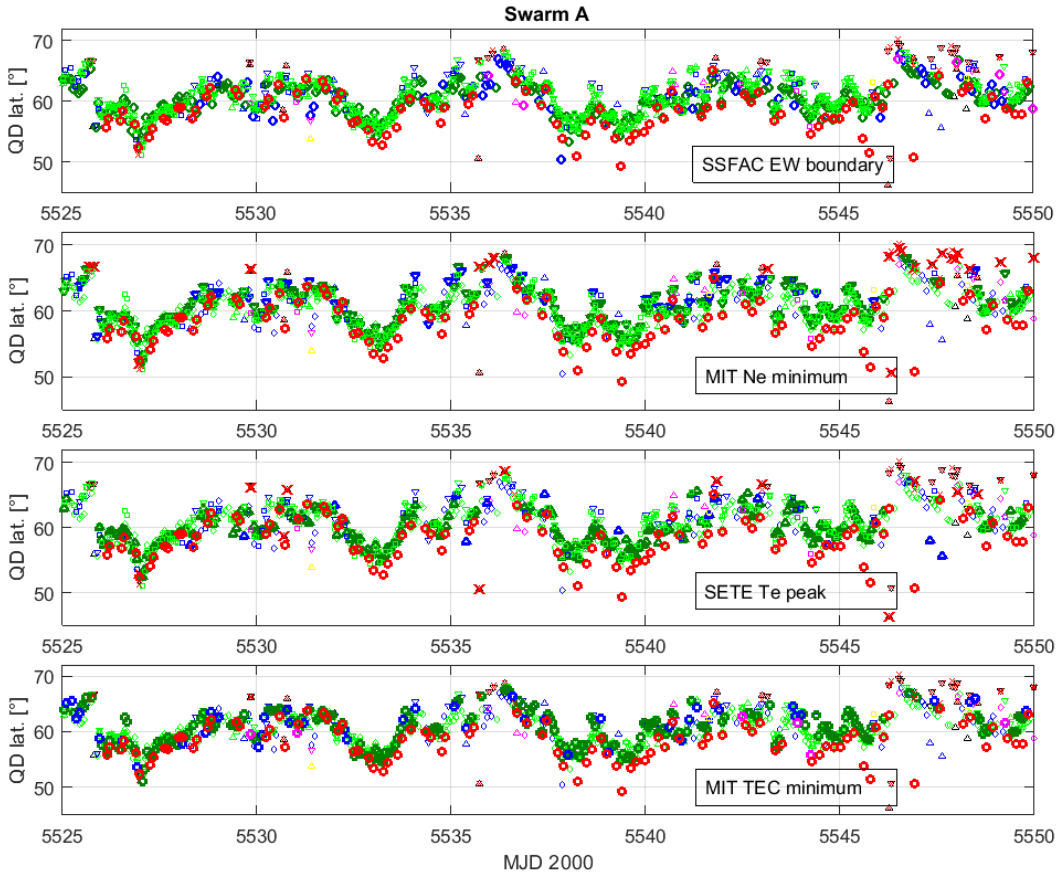


**Figure 5.3** Same as Figure **4.22** but for a different MJD interval complemented with the corresponding PP positions of the validating dataset.

These two properties of ESA densities can be used to calibrate the $N_{pot}$ density proxy in the plasma trough. In the plasmasphere, a saturated plasmasphere model is enough for a rough calibration. For this purpose, we used the recently published EMMA model ([RD-5]). Since we are interested in the location of the PP only, where the plasma density drops by an order of magnitude, there is no need for accurate calibration. According to [RD-4], the plasma density can be estimated within a factor of two by the above method. Even if the accuracy is poorer, it is likely good enough to find the PP.

Overall, we have inferred 9586 PP positions from the data recorded by the six spacecraft for the years 2014-2017. The share of the individual satellites of these PP crossing data is as follows: RBSP A: 3555; RBSP B: 2447, ERG: 583, THEMIS A: 292, THEMIS D: 1358, THEMIS E: 1351. The distribution of the PP positions is shown in Figure 5.4. The data cover the L = 1.8-7.6 range with a good coverage for L = 2.5-5.75 range.

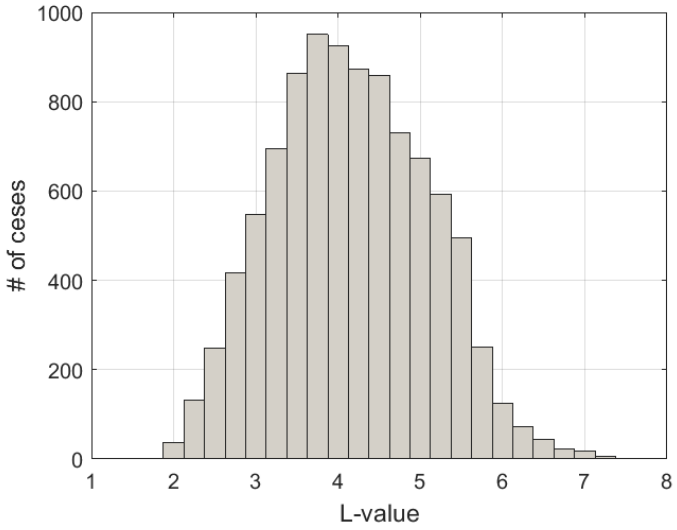


**Figure 5.4** Histogram of the PP positions used for validation.

## 5.1 MITx_LP_2F

First, the difference between the PP location and the MIT minimum has been derived. Since the MIT observations are night time observations, the comparison is restricted to the night side. Earlier studies have found that these boundaries in general are closely located. For a direct comparison we used the L-value of the field line passing through the location of the satellite observing the phenomena investigated.

The MIT minimum is on average inside of the PP (Figure 5.5). The distance is typically below 0.5 Earth radii, decreasing with increasing geomagnetic activity. There is no strong dependence on MLT, how-ever. This may be a bit surprising at a first glance, since the MIT location has a strong MLT dependence as was shown, e.g., in Figure 4.6. This result suggests that there is a similar dependence for the PP, too. Indeed, the plasmasphere has a bulge on its dusk side, and hence, the PP tends to near the Earth to-ward midnight. The formation of the bulge is related to the formation of a stagnation zone, where corotation related and magnetospheric convection related electric fields balance each other. This process is coupled to the formation of the MIT in the ionosphere.

The plasmasphere, more precisely, the main body of the plasmasphere is co-rotating with the Earth, while the bulge (plasma in the stagnation zone) stays at the dusk side. The consequence of the corotation is that

the temporal variation of the night time PP position appears with a delay at later MLTs. This can be checked by calculating the cross-correlation of the time variations. To perform the correlation, we need two suitable time series. Both the PP and the MIT data set have uneven and different sampling. The MIT time series was resampled to match the PP sampling in the following way. First, for every PP position we calculated the mean of the MIT positions that were within 2 hours from the PP observation considered. Then the correlation between the two time series was calculated. The correlation calculation was done separately for different MLTs. The corresponding correlation coefficients are plotted along the dashed line (i.e., at zero-time lag) in Figure 5.6. As seen, the correlation is in general high at night and low at dusk (in the lack of daytime MIT observations, the correlation cannot be calculated for most of the daytime).

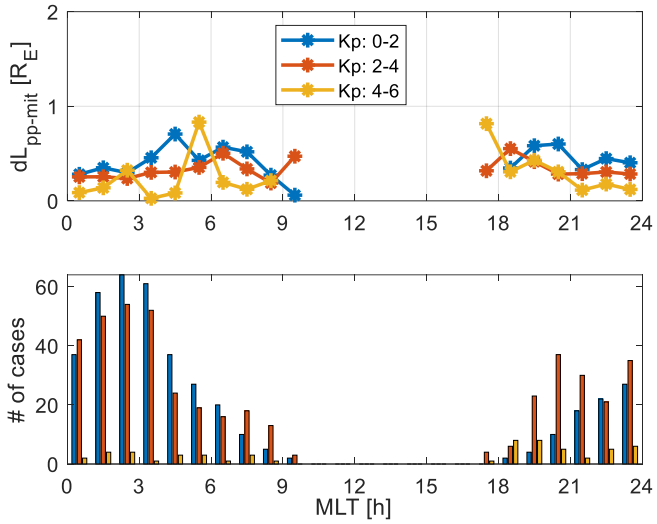


**Figure 5.5** (top) Average distance of the PP and the MIT minimum vs MLT for three different level of geomagnetic activity, (bottom) histogram of the observations considered.

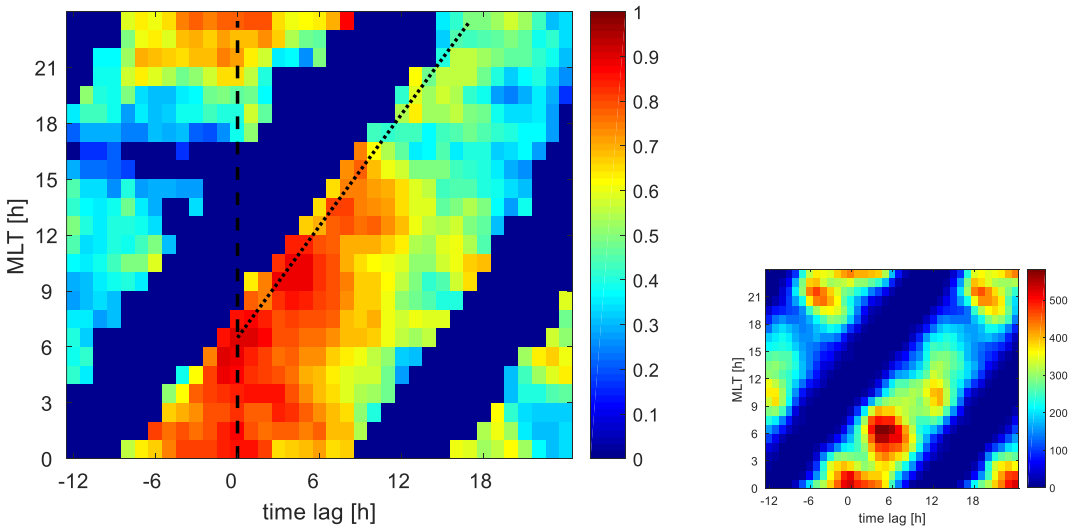


**Figure 5.6** (left) MLT dependent cross-correlation matrix calculated between PP and MIT position variations, (right) distribution of the data used for the statistics.

Then the calculation was repeated with a time-shifted MIT data set. The time shift (lag) varied be-tween -12 h (PP leads by 12 h) and 24 h (PP variation lags behind MIT variation by 24 h) populating the correlation matrix shown in Figure 5.6 (left). All temporal tolerance (time difference allowed) including that of the MLT is set to 2 h.

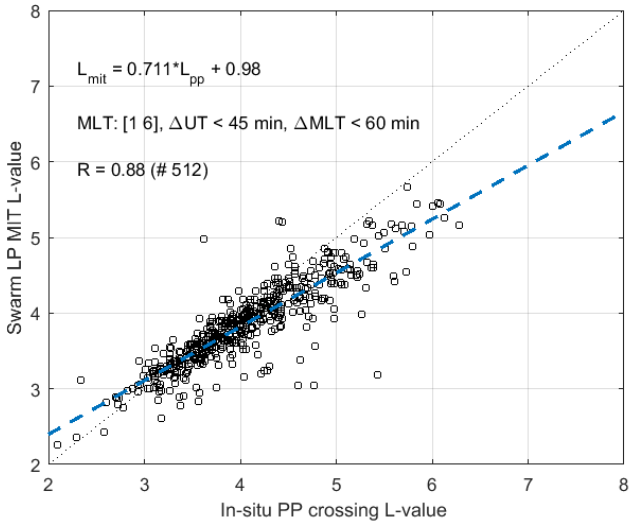


**Figure 5.7** Correlation between the in-situ PP observations and the MIT locations between 01-06 MLT.

As expected, in the midnight-post-midnight sector the variation of the two boundaries is close to simultaneous, i.e., the correlation maximises near -1-0 h time lag. At later MLTSs the PP variation lags behind the night time MIT dynamics. The link between the two boundaries is the strongest in the post-midnight MLT sector (Figure 5.7). From around 6 h MLT toward noon and beyond, the variations propagate by corotation, i.e., around 1 h MLT during 1 h time. In part due to the applied 2 h time tolerance (condition for simultaneity both in UT and MLT), the maxima are spread, even toward negative lags. Another reason for the spread is that both processes producing the MIT and the PP share a common driver rather than one of them is the driver of the other one. Both boundaries respond by some varying time delay causing uncertainties in their phase difference. The pre-midnight decrease of the correlation strength (e.g. at zero lag) indicates that the average correspondence between the bulge boundary and the MIT may not hold case by case.

## 5.2 MITxTEC_2F

A similar analysis was performed also on MIT minima derived from TEC observation, as well. The results are also very similar and summarised in Figure 5.8, Figure 5.9 and Figure 5.10.

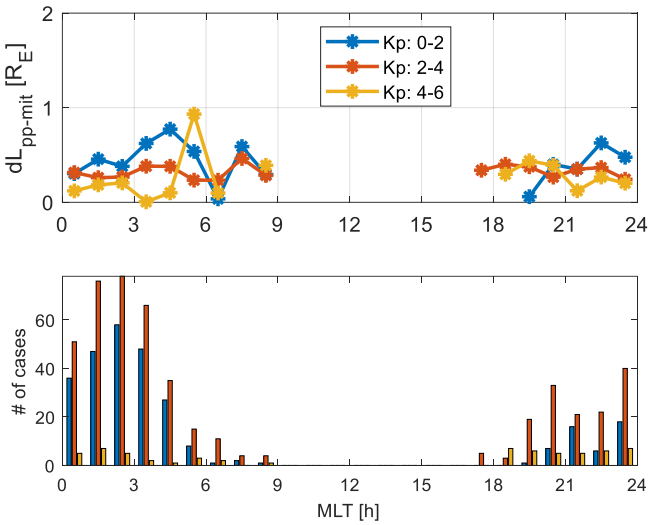


**Figure 5.8** Same as Figure **5.5** but for the MITxTEC product.

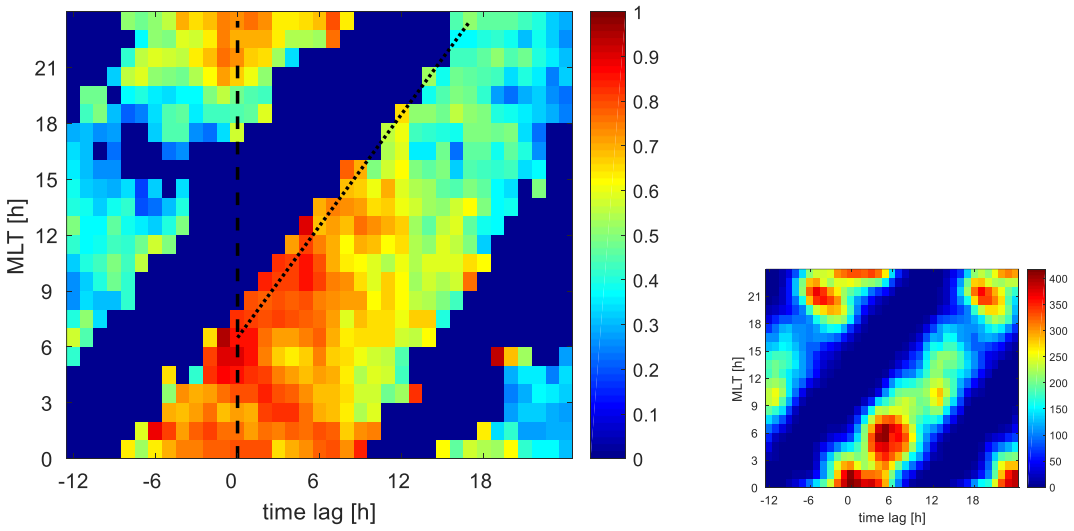


**Figure 5.9** Same as Figure **5.6** but for the MITxTEC product.

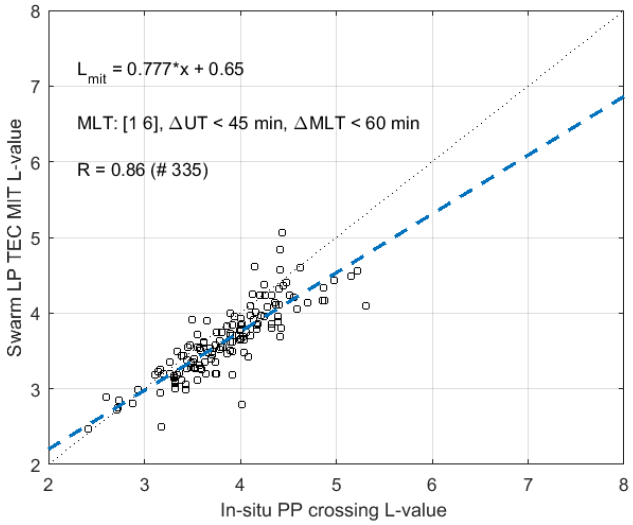


**Figure 5.10** Same as Figure **5.7** but for MITxTEC.

## 5.3 PPIxFAC_2F

The same analysis for the PPIxFAC product yielded a different result. To derive Figure 5.11 we made use of the SSFAC boundary model introduced in section 4.4. From an actual observation of the boundary and by means of the model, the position of the SSFAC boundary at any MLT can be calculated. Hence, the difference between the PP and the SSFAC boundary can be calculated with full MLT coverage even if the MLT-coverage of the SSFAC observations is limited. The difference in this case shows a clear bulge (Figure 5.11). Moreover, the bulge location moves toward earlier MLT with increasing Kp. This is a known behaviour of the PP. At all MLTs, the SSFAC boundary is inside the PP.

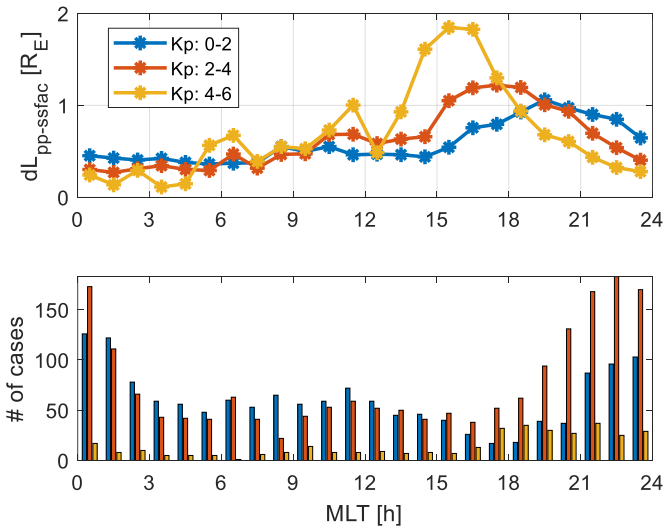


**Figure 5.11** Same as Figure **5.5** but for the PPIxFAC product.

This result also indicates that the nature of the link between the SSFAC boundary and the PP is different from the link between the MIT and the PP. The SSFAC boundary that is often observed in the post-dusk sector does not follow the bulge (nor the MLT dependence of the MIT as was shown earlier).

From the post-midnight (0-3) MLT range the average difference can be derived as a function of Kp:

$$dL_{pp-ssfac}(Kp) = -0.075Kp + 0.53 \quad \text{Eq. 5.3-1}$$

or as a function of the SSFAC boundary position itself (that is very sensitive to the geomagnetic activity):

$$dL_{pp-ssfac}(L_{ssfac}) = 0.072L_{ssfac} + 0.05 \quad \text{Eq. 5.3-2}$$

Since the latter is available at once, as the observation is made, we use this formula to adjust the midnight SSFAC boundary position. We call the adjusted value the PP index (PPI). This is derived in two steps: 1. from the actual SSFAC observation the midnight SSFAC boundary position is derived using the SSFAC boundary model; and 2. the derived midnight SSFAC position is adjusted by the above formula (the dL difference from the formula is added to the SSFAC position). The PPI thus yields a proxy for the midnight PP location whenever the SSFAC boundary is observed.

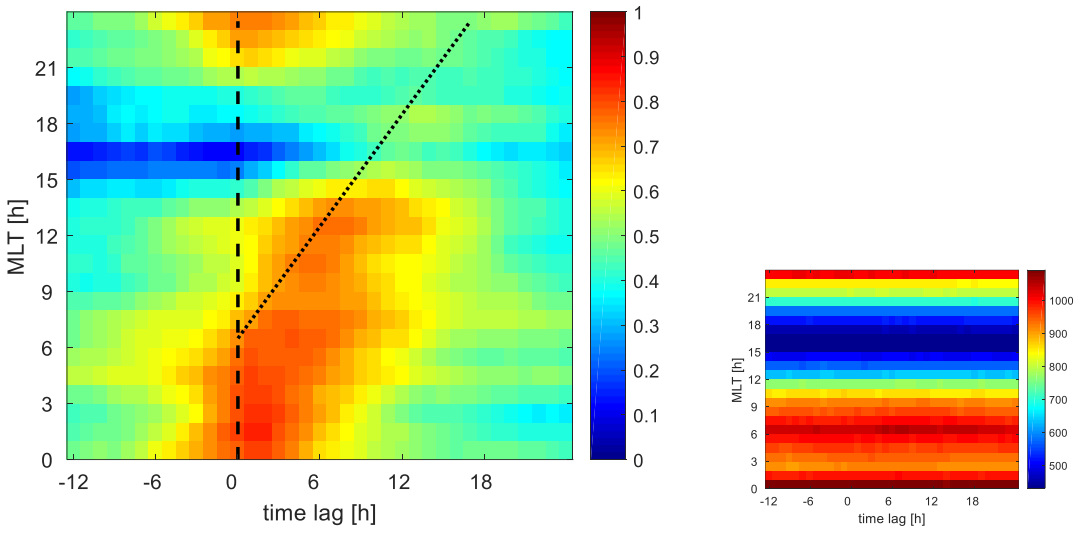


**Figure 5.12** Same as Figure **5.6** but for the PPIxFAC product.

Figure 5.12 is similar to but also somewhat different from Figure 5.6 and Figure 5.9. While MIT positions were compared with simultaneous PP observations that are close also in space (MLT difference is limited), here the in-situ PP observations are correlated with Swarm PPI that is derived from SSFAC boundary observations at any MLT. Thus, no condition on the MLT difference is needed. As a result, the correlation matrix is fully populated. The figure also clearly shows the corotation-related effects on the dayside. We believe that this is because the SSFAC boundary is coupled to processes that form the new plasmapause in the near-midnight–post-midnight sector. It means that the new PP is formed in the 21-06 MLT sector and appears on the dayside as a result of corotation.

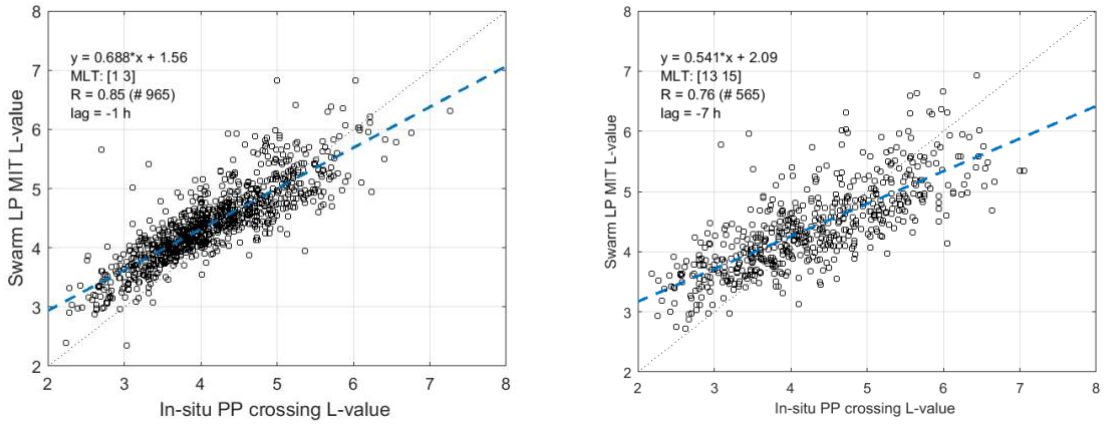


**Figure 5.13** Correlation between the time shifted PP observations and Swarm PPI.

In Figure 5.13, the correlation between true PP and Swarm PPI is shown for two MLT sectors (MLT of PP observations). Swarm PPI has been smoothed by a 7-point running averaging. The correlations are calculated at the time lag that provided the strongest correlation. This was 1 h for the post-midnight (1<MLT<3) example, and 7 hours for the post-noon (13<MLT<15) example. In the latter case, magneto-spheric PP observations were compared with Swarm PPI recorded seven hours earlier (!). The correlation strength is 0.9 and 0.8 in the cases considered. Swarm PPI observations in this late MLT sector are sparse, and they do not correlate well with simultaneous PP observations made at close MLTs. This finding is again in support of the previously introduced corotation origin of the dayside PP.

# 6 Discussion and conclusions

The validation proved the consistency of the products and revealed some of their limitations by comparing product copies derived from the side-by-side flying satellite pair. In general, the agreement was found satisfying between the products compared. The difficulty in finding the EW edge of MIT and SETE stems from the nature of the phenomenon itself, i.e., in many cases the EW wall is poorly developed, the transition from the low latitude density values toward the MIT minimum is often very smooth, at least at the altitude of the observation. This is increasingly true for the TEC profiles. The detection of SETE and its edges, especially its EW edge is also often challenging, in part due to the small-scale structures / high frequency 'noise' present in the Te data. In spite of this, the Te data was found very useful in characterising the MIT and the sub-auroral ionosphere. The SSFAC boundary product is based on a small-scale field-aligned current (up to some 10 km spatial scale). The spread of the Swarm C-A difference here can be attributed to real small-scale variations between the two locations. The accuracy estimates in [AD-2] are derived from the above Swarm A-C comparisons.

The comparisons of the three PRISM products with each other, as well as with other products (AOB) and boundaries (SZA-terminator) (see [AD-3]) were useful not only to assess and quantify the quality of the products but also supported the definition of the quality flags. Quality flags are essential for the proper interpretation of the data. The most important flags are the main flags for each of the three products. Products with main flag 3 or 2 are mostly safe to be used even for event analysis, while records with a main flag 1 or 0 are recommended only for inclusion in statistical analysis.

Validation with PP positions inferred from in-situ plasmaspheric observations proved also the great potential of all three products for monitoring plasmasphere dynamics at LEO. A simple formula is derived to account for the difference between the SSFAC boundary and the PP at midnight. This formula is used in the derivation of PPI, the Swarm plasmapause index.